Acta Astronautica 237 (2025) 460–475

Contents lists available at ScienceDirect

Acta Astronautica

journal homepage: www.elsevier.com/locate/actaastro

First tests of a laser ice drill for the exploration of interplanetary ice and icy soils

Martin Koßagk [a,*], Leo Peiffer [a], Lukas Mohr [a], Martin Tajmar [a,b], Tino Schmiel [a]

[a] Technische Universität Dresden, Institute of Aerospace Engineering, Dresden, Germany
[b] Faculty of Space Technologies, AGH University of Krakow, Poland

ARTICLE INFO

Keywords:
Icy moons
Laser drilling
Comet
Melting probe
Dusty ice
Laser ice drill

ABSTRACT

The exploration of icy moons and other icy regions such as permanently shadowed lunar craters, Martian polar caps or comets is of great scientific interest, as they might offer life-friendly environmental conditions or can serve as resource deposits for human exploration. In contrast to conventional melting probes, this work presents a laser ice drill, which drills a 6.15 mm diameter hole in the ice and drives the resulting gases and non-volatile additives from the bottom of the hole to the surface for analysis purposes. To demonstrate the concept, various types of ice with dust fraction up to 96.6 wt% were drilled in a laboratory setup. The tests were carried out at vacuum pressures in the 100 Pa range and ambient temperature. The drilling depth was simultaneously tracked with a laser rangefinder, so that a depth assignment of the ejected substances was possible. During the drilling tests, melting speeds of up to 1.7 m/h at 12.7 W laser power were achieved in pure granular ice and 1 m/h at 19.7 W in clear ice. In dusty ice, however, even higher drilling speeds were achieved without increasing the laser power. The melting rates of all drilling experiments are simulated in good agreement with a thermal model.

Nomenclature

A	$[\mathrm{m}^2]$	irradiated spot area
c_p	$[\mathrm{J/kg \cdot K}]$	heat capacity of ice
E_drill	[J]	drilling energy
E_in	[J]	energy introduced into the ice
E_loss	[J]	energy losses
h	[J/kg]	sublimation enthalpy of ice
m	[kg]	ice mass
m_probe	[kg]	ice sample mass
p	[Pa]	ambient pressure in vacuum chamber
$p_\mathrm{subli\_ice}$	[Pa]	sublimation pressure of ice
P_L	[W]	laser power
s	[m]	drilling depth
t	[s]	time
$T_\mathrm{subli\_ice}$	[K]	sublimation temperature of ice
v_drill	[m/s]	drilling speed
V	$[\mathrm{m}^3]$	volume of ice
V_probe	$[\mathrm{m}^3]$	volume of ice sample
ΔT	[K]	temperature difference
η	$[-]$	loss due to reflectance on ice surface
ρ	$[\mathrm{kg/m}^3]$	density of ice sample
$\rho_\mathrm{real\_ice}$	$[\mathrm{kg/m}^3]$	density of dusty ice sample, considering only the ice content
ω_dust	$[-]$	dust fraction in ice sample

Acronyms/Abbreviations

AUV	Autonomous Underwater Vehicle
SIPR	Subsurface Ice Probe
DLP	Direct Laser Probe
SIPR	Subsurface Ice Probe
SNAP	Systems Nuclear Auxiliary Power
RTG	Thermoelectric Radioisotope Generator

1. Introduction

The exploration of ice in the solar system is of great interest. Whether it is ice in lunar craters to supply astronauts with water [1] or the mining of water ice in asteroids to produce fuel [2,3]. In addition, ice worlds such as Europa and Enceladus with their supposed oceans under the ice sheet are of great interest to science [4], since they can potentially harbour life. Accordingly, various melting probes have been developed and tested on glaciers, Greenland Ice Sheet and in the Antarctic to prepare them for the exploration of ice worlds and their oceans.

The melting probe IceShuttle Teredo is designed to melt its way

---

* Corresponding author. Marschnerstr. 32, Dresden, 01307, Germany.
E-mail address: martin.kossagk@tu-dresden.de (M. Koßagk).

https://doi.org/10.1016/j.actaastro.2025.08.049
Received 16 March 2025; Received in revised form 8 August 2025; Accepted 25 August 2025

through the ice crust of an icy moon to the ocean below and deploy an autonomous underwater vehicle (AUV) there. The AUV will study the ocean and use the melting probe as a port for energy supply and data transmission [5]. Similarly, the SPINDLE melting probe will deploy an AUV into the water beneath the ice to collect samples and search for life [6]. Other melting probes carry payloads on board to explore the ice.

For example, the Cryobot carries a camera to explore the ice structures and sediments and a UV spectrometer to search for biostructures [7]. The IceMole uses a hollow ice screw at the tip of the melting head to collect samples. Thus, subglacial samples were collected from the Antarctic brine body of the Bloodfalls [8]. In contrast, the Subsurface Ice Probe (SIPR) pumps the meltwater through a Teflon tube to the surface for analysis. This creates an open melt channel, allowing the cable for energy, data and water transport to be unspooled from above. Field tests in the Greenland Ice Sheet and at the Athabasca Glacier showed drilling speeds of 1 m/h with a heating power of 250 W and a probe diameter of 7.5 cm [9]. The Recoverable Autonomous Sonde (RECAS) reached a depth of 200.3 m with an average drilling speed of 1.85 m/h during field tests in East Antarctica. It had a diameter of 180 mm and a maximum heating power of 8.82 kW [10]. The Ice Diver achieved melting speeds of 2.4 m/h with a heating power of 2.15 kW respectively 6.6 m/h at 4.5 kW and a melting head diameter of 6.5 cm in field tests in the Greenland Ice Sheet [11]. The 12 cm diameter Cryobot melts its way through the ice at 0.35–0.6 m/h using a 1 kW melting head. To do this, it uses either the heated melting head or a hot-water jet nozzle, which jets previously heated water onto the ice [7]. The 25 cm diameter VALKYRIE melting probe also uses these two melting modes. With 5 kW heating power, it achieves a drilling speed of 0.9 m/h in hot-water jetting mode during field tests in the Matanuska Glacier [6]. The energy supply was ensured via laser, which was guided from the surface to the sample via a fiber optic cable and irradiated the melting head from the inside. The fibre optic cable is unspooled inside the melting probe [6]. The internal spooling mechanism is necessary because the melting holes behind the melting probes refreeze. As a result, the melting probes move through the ice in their own bubble of meltwater. This bubble also serves as a water source for the hot-water jetting mode [12]. The THOR melting probe was used to simulate a 700 m descent in a water bath at −0.5 °C with a hot water jet system [13]. Stone et al. [12] has demonstrated with several miniaturized melt samples in a cryovacuum chamber at approx. 80 K and a pressure of 0.13 Pa that refreezing of the ice channel also occurs under vacuum conditions. His experiments also showed a higher melting rate in the hot-water jetting mode compared to contact heating with a melting head. Paula do Vale Pereira et al. [14] were also able to observe the closing of the drill channel during melting tests with various melting probes at ice temperatures of 79 K–253 K in a vacuum. Further melting tests in compact snow and ice under cryovacuum conditions were carried out by Kömle et al. [15,16]. And melting tests under atmospheric and vacuum conditions at temperatures between −25 °C and −55 °C were performed by Treffer et al. [17]. Talalay et al. [18] also conducted melting tests in ice with different melting head shapes, heating powers and temperatures between 223 K and 263 K (see Table 1).

Experiments by Kaufmann et al. [19] showed that a good thermal contact between the tip of the probe and the ice is necessary. Under terrestrial conditions, this is always provided by the formation of meltwater. Under vacuum conditions, however, the ice sublimates. The lack of meltwater therefore minimizes the thermal contact and slows down the progress of the probes. For better thermal contact with the ice, the IceMole uses its hollow screw at the tip of the melting head to pull itself against the ice. This also enables the IceMole to move upwards through the ice against gravity, as tests in the Morteratsch Glacier have shown [20]. With a cross-sectional area of 15 × 15 cm^2 and a heating power of 2.4 kW at the melting head and a further 2.4 kW in the side heaters, a melting speed of 1 m/h was achieved. The Direct Laser Probe (DLP) directed the laser light of a 1070 nm ytterbium fiber laser directly onto the ice for better coupling of the melting probe to the ice [6]. This drilled a hole in the ice where the drill head with a diameter of 3.2 cm fits in. With 2.5 kW laser power, 12 m/h melting speed were achieved in a 1 m block of ice and later 22 m/h with 5 kW (see Table 1). Here, the laser outlet window of the fiber was pushed into the hole in order to ensure a constant and close distance to the ice surface. This was necessary to minimize the layer of water between the laser head and the ice and thus minimize absorption losses in the water.

Table 1
Summary of several melting experiments and the drilling speed achieved under laboratory conditions with different sample diameters, heating powers, power integration technologies into the ice and ice temperatures.

Published by	Velocity [m/h]	Heating Power [W]	Probe diameter [mm]	Melting technology	Laboratory environment
Zimmerman 2001 [7]	0.28	200	80	contact melting	vacuum; −20 °C ice
	0.59	1100	46		vacuum; −195 °C ice
Stone 2023 [12]	0.45	2590	70	contact melting	vacuum; −190 °C ice
	0.7			hot water jet	
Treffer 2006 [17]	0.087	600	115	contact melting	vacuum; −55 °C ice
	0.125				atmosphere; −25 °C ice
Talalay 2019 [18]	1.4–2.9	2400	55	contact melting	atmosphere; −20 °C ice
Stone 2018 [6]	12 22	2500 5000	32	Laser melting	atmosphere; −26 °C ice
Sakurai 2016 [21]	2.9	6.28	4	Laser melting	atmosphere; 0 °C ice

Drilling tests at ambient temperature without moving the laser were carried out by Sakurai in 2016 [21]. Here, a $\mathrm{CO_2}$ laser with a spot diameter of 4 mm was used to drill through a 13 cm block of ice. The holes were drilled horizontally to ensure drainage of the produced meltwater. This enabled a drilling speed of 2.9 m/h to be achieved with 6.28 W laser power. Mah et al. [22] also drilled holes in clear ice samples with a maximum length of 30 cm. He used a collimated 1064 nm laser beam with a spot diameter of 30 mm and achieved drilling speeds of 9 m/h at 1 kW and 75.6 m/h at 10 kW laser power. The tests were designed in such a way that the melt water flowed continuously out of the borehole.

Dust layers in the ice were also drilled through with melting probes. For example, Kömle et al. [16] drilled through layers of dusty ice with a thickness of a few centimetres using a 60 mm melting probe and heating power of between 85 and 115 W. In the process, the melting head temperature increased and the melting rate slowed down. The IceMole was also able to drill through 3 obstructive layers of sediment and sand in the Morteratsch glacier [23].

The main problem of melting probes in the context of extraterrestrial exploration is their high power and thus mass requirement. Nuclear energy sources are proposed as a solution to this problem. For VALKYRIE, a compact nuclear reactor system (Systems Nuclear Auxiliary Power: SNAP) or a Topaz reactor with an average output of 20–100 kW is proposed [24].

A small nuclear reactor on the surface of the ice is also proposed for the IceMole, which supplies the IceMole with energy via a cable [25]. Also thermoelectric radioisotope generators (RTG) for melting are proposed [26]. The Cryobot was also envisaged to use the thermal power of an integrated RTG for melting [27]. The melting speed of the probes is determined by the available thermal power, the ice properties, thermal connection and probe diameter. While the thermal connection is well solved by encapsulating the melting probes in the ice, using ice screws, hot-water jets or lasers, the probe diameter poses a greater problem. Due to the spool mechanism and the transport payloads (AUV, camera, spectrometer, filter, etc.), it cannot be reduced as desired. In order to still ensure high volumes with small probe diameters, the melting probes are very long (Iceshuttle Toredo 6.75 m long [5]; Spindle 8 m long [2]), which detrimentally influences the design of both the transfer and the lander spacecraft. Apart from the dimensions of melting probes and their high-power consumption, the mass of the envisaged cable can also constitute a mission deal breaker for remote sites like Enceladus. The cable either restricts the possible exploration depths to only hundreds of meters or, depending on conductor cross section, exceeds the mass budget of the spacecraft.

This paper presents a new concept that enables high melting speeds despite low power requirements. For this purpose, a laser will be used which is stationed on the surface of the ice. Due to the low ambient pressure on icy moons [28], comets, Pluto [29] and the polar caps of Mars [30], and the exposed ice in these locations, it is possible that the laser could sublimate a hole in the ice. Cardell predicts that due to the low gravity of Mars and the low temperatures of the ice, the flow of the ice will not close the borehole to a depth of 3 km, whereas on Earth the flow of the ice would close a borehole at a depth of >300 m [31]. Accordingly, deeper boreholes could be possible on the icy moons. The water vapor generated during drilling flows towards the surface and can be collected there for later analysis or can be analysed using continuous measurement methods such as mass spectrometry or cavity ring down spectrometry (see Fig. 1). In order to be able to allocate the analysis data to a corresponding depth in the ice, the borehole depth is determined continuously with a laser rangefinder during the entire drilling process. The drilling laser operates at a wavelength of 1550 nm. At this wavelength, there are low reflections on the surface of the ice according to ECOSTRESS Spectral Library [32,33] and high absorption in the ice [34]. This enables a good thermal coupling into the ice. Due to the high absorption in the ice, the zone in which the energy is released is kept small, thus minimizing losses via heat conduction. The concept allows hole diameters of less than 1 cm and therefore a rapid drilling progress with low power requirements. Despite the fact that the sublimation enthalpy is 8.5 times higher than the melting enthalpy, the small hole diameter ensures a lower energy requirement. Furthermore, the system mass of an ice exploration mission can be highly reduced, as no kilometre-long cables are needed for the power supply and data connection between the melting probe and the lander.

However, the concept cannot take an UAV into an ocean under the ice. It is solely designed to analyse the ice crust. Obstacles cannot be avoided either. To conquer this issue, a preliminary exploration with radar instruments such as the SHARAD Instrument on the Mars Reconnaissance Orbiter [35] would be recommended. Alternatively, a new borehole could be drilled into the ice with a minimal angular deviation from the previous one. As the energy requirement is low, it should be possible to drill several boreholes in order to obtain a three-dimensional image of the additives in the ice crust and the ice density.

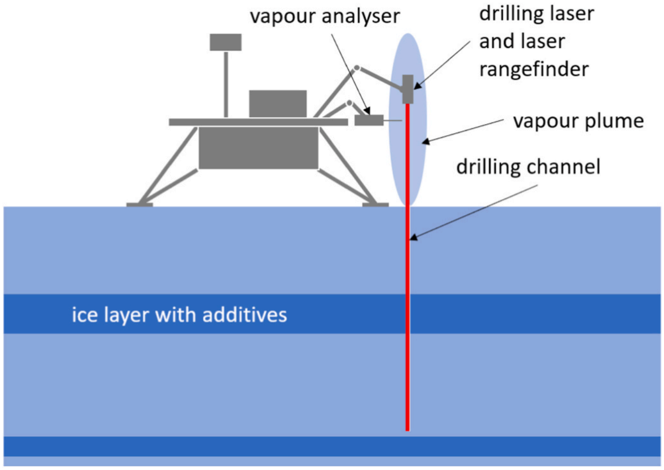

Fig. 1. Lander with ice laser drill, which sublimates the ice and creates a vapor plume. This plume can be analysed by additional instruments on the lander. A laser rangefinder collinear to the drilling laser measures the borehole depth and assigns the measurement results to a depth in the ice.

The experiments carried out here can only reflect the conditions on the icy moons to a limited extent. However, the ice samples were composed on the basis of knowledge about the surface composition of some icy moons and Mars. Since cryovolcanism prevails on some icy moons (Enceladus [36] and Europa [37]) and a continuous bombardment of charged particles also knocks ice grains out of the crust on Ganymede [38], the surfaces of the icy moons mentioned here are covered by deposits of granular ice. These presumably become denser with increasing depth and thus pressure due to their own weight. Therefore, samples of granular ice with different grain sizes and clear ice samples are examined in the following experiments. Due to the high silicate content of 55 %–80 % on Callisto [39], samples with different dust contents are also tested.

The following table provides an overview of the assumed ice grain sizes, as well as the prevailing temperatures and pressures. According to Murphy et al. [40], the sublimation temperature was determined according to the pressure and added to the table. It can be seen that the environmental conditions on the icy moons are close to the sublimation line of water ice. Accordingly, the experiments in the laboratory are also carried out close to the sublimation line (also added to the table).

This paper first presents the concept and the experimental concept verification setup. Clear ice samples were drilled with different laser powers under vacuum conditions, as well as granular ice with different densities and grain sizes. It could be shown that depth tracking is possible during the drilling process. To test whether dust in the ice poses an obstacle to the drilling process, ice samples with different types of dust, grain sizes, densities and with dust mass fractions of 50–96.6 wt% were subjected to the drilling tests. Due to the high dust concentrations of these ice samples, other fields of application arise in addition to icy moons, Pluto and the polar caps of Mars, such as comet ice and ice in lunar [49] and Mercury craters [50]. The measurement results obtained are then compared with a thermal model and subsequently discussed.

2. Materials and methods

2.1. Test bench setup

A laser (ELM-20) from IPG with a wavelength of 1550 nm is used to drill into the ice. It has a spot diameter of 4.1 mm and a divergence angle of 0.49 mrad. A beam expander (BXZ-1550-1-4x) from Wavelength Opto-Electronic is used to expand the beam by a factor of 1.5. This laser beam is collinearly combined with the laser beam of a laser rangefinder via a dichromatic mirror (DMLP1000 from Thorlabs). The laser of the rangefinder (PC LA-100-OEM) from Hillos has an elliptical spot with the dimensions of 4 × 5 mm^2 at a distance of 10 m and a wavelength of 655 nm. Both laser beams are guided through a borosilicate sight glass (110GS040) from Pfeiffer Vacuum. In the vacuum chamber, both laser beams are directed vertically into the respective ice sample via a silver-coated mirror (PF10-03-P01) from Thorlabs (see Fig. 2). In order to sublimate the ice with the 1550 nm laser, the pressure in the chamber must be below the triple point of water. In order to maintain this pressure despite the constant addition of water vapor by the laser, a dual-stage vacuum pump (VRD-65) with a displacement speed of 65 m^3/h from Hositrad is used. The pressure is monitored using a Pirani sensor (PT R43 131 A) from Pfeiffer Vacuum.

2.2. Conduct of the experiment

2.2.1. Ice samples

Three different types of ice samples are used for the drilling tests. For the first type, demineralized water is frozen in a sample tube to obtain a clear ice sample with some air bubbles. For the second type of sample,

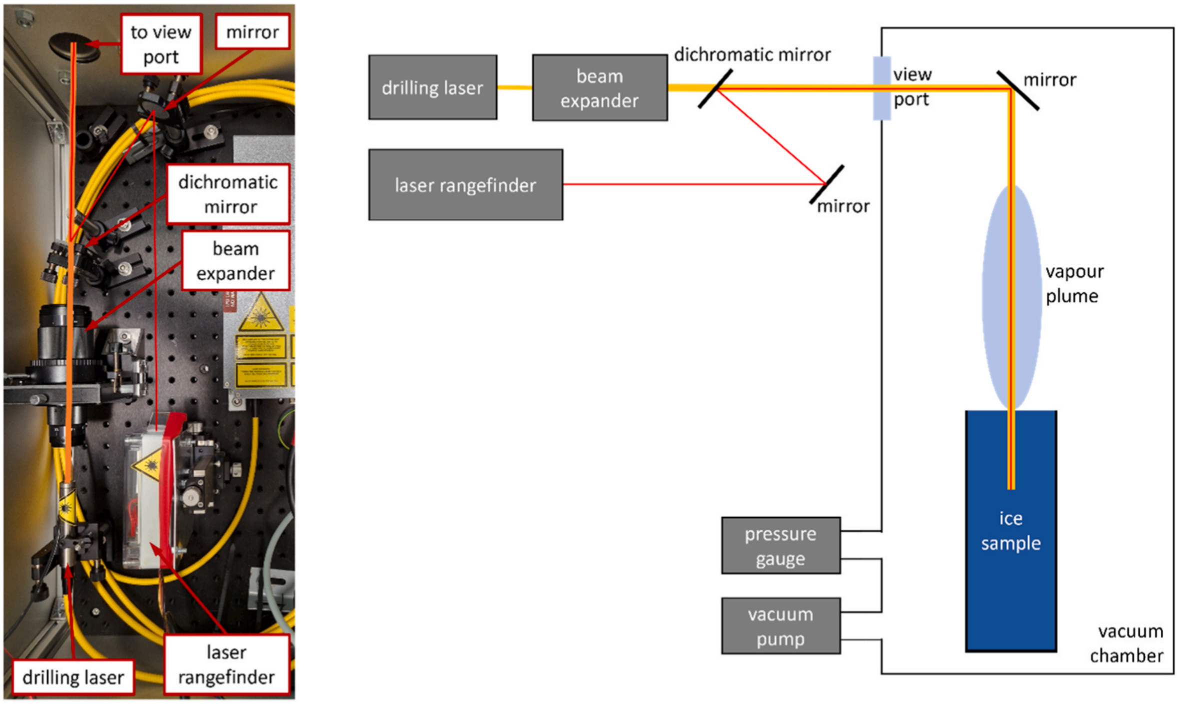

Fig. 2. Optical setup of the drilling laser and laser rangefinder (left); Schematic of the test bench setup for drilling ice samples in a vacuum with a laser, including borehole depth measurement using a laser rangefinder (right).

demineralized water is sprayed into a liquid nitrogen bath similar to Pommerol et al. [51] and Klinger et al. [52]. A pneumatic ZERSTAUB M5 B atomizer with Venturi effect was used to generate water droplets in order to produce shock-frozen spherical grains in the range between <0.1 mm and 5 mm. This size of the ice particles is in the order of magnitude expected on the icy moons (see Table 2). With the help of a sieve tower consisting of nine stackable components, the ice grains were separated into different size classes. The stainless-steel sieves used for this had the following mesh sizes: 5 mm, 2 mm, 1 mm, 0.77 mm, 0.5 mm, 0.33 mm, 0.2 mm and 0.1 mm. The sieving process was supported by manually shaking the tower and rinsing with LN_2. The contents of the sieve stages were poured into separate sample tubes and temporarily stored in the freezer until drilling. The third sample type also consists of granular, sieved ice, which is mixed with various types of dust to form an inter-mixture according to Poch et al. [53]. The dust types were cooled before mixing and are listed in Table 3. The mass fraction of the dusty material in the dust-ice samples ranged from 50 wt% to 96.6 wt%.

Before drilling the samples with granular ice, the filling level in the sample tube and its mass are measured in order to determine its density. To prepare the dusty ice samples, the dust and ice fractions are weighed and mixed together with liquid nitrogen until the liquid nitrogen had evaporated. The dust-ice mixture is then filled into the sample tubes and its volume and mass are determined.

Table 2
Ambient conditions of selected celestial bodies and vacuum chamber conditions.

Celestial body	Surface pressure	Surface temperature	Sublimation tempera-ture at surface pressure	Particle diameter
Europa	1E-7 Pa [41]	110–130 K [42]	136 K	0.005 to 1 mm [42]
Callisto	7.5E-7 Pa [43]	85–160 K [44]	143 K	0.2 to 0.5 mm [39]
Ganymede	1E-5 Pa [45]	75–150 K [44]	152 K	0.05 to 1 mm [38]
Mars	About 600 Pa [46]	134 K–310 K [47]	273 K	1 to 40 mm [48]
Vacuum chamber	About 100 Pa	250 K–273 K	253 K	<0.1 to 5 mm

Table 3
Additives mixed with granular ice for sample preparation.

Type of dust	Grain size	Mass fraction in the dust-ice mixture
Basalt	0.5–1 mm	75 wt%
	0.1–0.6 mm	90 wt% and 75 wt%
	<0.3 mm	75 wt%; 66 wt% and 50 wt%
	<0.2 mm	75 wt%
Quartz	0.1–0.6 mm	96.6 wt%; 90 wt% and 75 wt%
	0.1–0.25 mm	95 wt%; 90 wt%; 75 wt% and 50 wt%
	<0.2 mm	75 wt%
Garnet	0.4–0.8 mm	75 wt%
Granite	0.5–1 mm	75 wt%
	0.1–0.3 mm	90 wt% and 75 wt%
	<0.1 mm	75 wt%
Copper	<0.045 mm	75 wt%
Pumice	<0.25 mm	96.6 wt% and 75 wt%
Bentonite	<0.063 mm	50 wt%; 78 wt% and 89 wt%

2.2.2. *Laser power measurement*

As the drilling laser is guided through a viewing port and via a mirror, there are absorption losses in the laser power. The losses due to insufficient reflection of the mirror are caused in particular by ejected material from the drilling process which contaminates the mirror surface. Therefore, the laser power is determined before and after each drilling attempt series and an average value is determined for the test evaluation. For all laser power measurements, the ice sample is temporarily replaced by a laser power meter (S425C-L) from Thorlabs.

2.2.3. *Drilling process*

The ice samples are stored in a freezer at approx. −20 °C before measurement. For the drilling tests, they were placed in the vacuum chamber at room temperature and then evacuated. When the vacuum chamber is evacuated, the water ice sublimates and cools the ice sample surface. As soon as the pressure is in the range of 100 Pa, the drilling laser is switched on. This causes the pressure in the vacuum chamber to rise again. The higher the laser power used, the greater the increase in pressure. As only the top of the cylindrical ice sample comes into contact with the vacuum, only this is cooled, while the lower part of the ice sample heats up. According to Feistel and Wagner [54], an ice temperature of −20 °C prevails in a vacuum at 100 Pa. With a reference ice sample, which was evacuated together with the clear ice sample to be drilled, it was possible to measure −23 °C at a depth of 1 cm below the surface and 0 °C at a depth of 1 cm above the reference sample bottom. The measurement was carried out using three thermocouples frozen at different depths. During drilling, the formation of meltwater at the bottom of the clear ice sample due to the warm environment and no contact to the vacuum was also observed.

During evacuation, the laser rangefinder measures the distance to the ice surface and thus determines the starting point for the drilling process. As soon as the drilling laser drills into the ice, the borehole depth is measured. When the drilling laser reaches the bottom of the sample, a constant distance to it is usually measured. However, if there is a liquid water reservoir at the bottom of the sample, water rises in the drill channel as soon as it is drilled into. As a result, the laser rangefinder measures any depth between the sample surface and the sample bottom. If the drilling test is continued, the measured depth increases again until the laser beam of the laser rangefinder finally reaches the bottom of the borehole (see Fig. 3 blue curve).

2.2.4. Post-processing

The average drilling speed in the respective ice sample is required for the evaluation. The data from the laser rangefinder is used for this (see Fig. 3). The distance is measured every 0.5 s, whereby occasional errors in the laser rangefinder - due to unsuitable reflectivities of the borehole bottom, and the deflection mirror - reduce the measurement frequency. The missing distance values due to the error output are reconstructed in 0.5 s time intervals using the remaining data by linear interpolation. The drilling speed between the successive distance points is then determined. As the drilling speed is quite slow, and the value of the laser rangefinder can fluctuate by 2.7 mm around the true distance value, the drilling speed is subject to strong noise. Therefore, the average speed of all speed increments is determined for further consideration.

2.3. Thermal model

The laser power, the sample density and the ice temperature have a major influence on the melting rate. In order to interpret the drilling results and to deduce implications for the use on extra-terrestrial bodies, they are simulated using a thermal model. For this purpose, an energy equilibrium

$$E_{in} = E_{\text{drill}} + E_{loss} \tag{1}$$

is set up, in which the energy E_{in} is introduced into the ice by the laser power P_{L} for a certain time t via the spot area A of the laser.

$$E_{\text{in}} = (1 - \eta) \cdot P_{\text{L}} \cdot t \tag{2}$$

A fraction of the energy is reflected by the ice surface and is not available to the drilling process. According to Meerdink et al. and Baldridge et al. [32,33], the reflectance η for ice is 1.6 % at a wavelength of 1550 nm. For a bulk of ice particles, the reflectance also depends on the particle size. According to Poch et al. [55], the reflectance for a bulk of ice particles with a size of 67 μm at a wavelength of 1550 nm is 8.5 %. The energy applied to the ice is used as the drilling energy E_{drill} to heat a certain volume of ice with the heat capacity c_{p} and the mass m from its current temperature by the temperature difference ΔT to the sublimation temperature and to sublimate this volume of ice mass m with the sublimation enthalpy h.

$$E_{\text{drill}} = c_{\text{p}} \cdot \Delta T \cdot m + h \cdot m \tag{3}$$

The energy loss E_{loss} is caused by heat conduction. Mass that is heated does not have to sublimate immediately. However, it can do so in the next time step if laser power is applied again. In the meantime, it can transfer its energy to the ice below or next to it via thermal conduction. If heat is conducted into the ice underneath, it is preheated and sublimated in the next or subsequent time step. The energy is not lost here. However, if it is conducted into adjacent ice that is not captured by the drilling laser in the future, this energy is lost. The loss via heat conduction is neglected for the modeling of the drilling experiments carried out here for the following reasons.

1. The laser impact zone is very flat. According to Warren et al. [28], ice has an absorption coefficient of 3441 m^{-1} at 1550 nm. According to Lambert Beer’s law, 90 % of the laser power is absorbed within 0.7

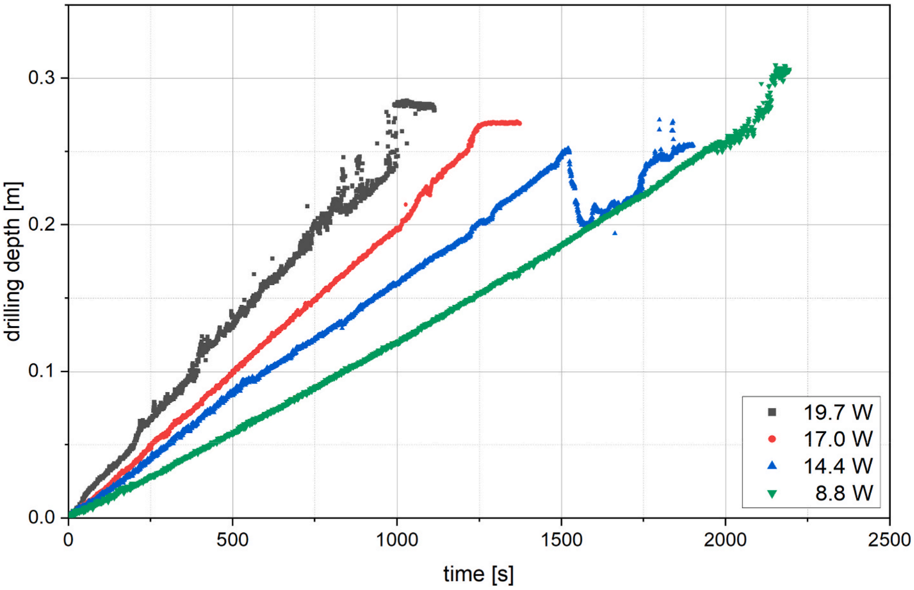

Fig. 3. Drilling progress in clear ice at different laser powers. Blue curve: Drilling into a liquid reservoir at the bottom of the ice sample, resulting in temporarily incorrect borehole depth measurements. (For interpretation of the references to colour in this figure legend, the reader is referred to the Web version of this article.)

mm and 99 % of the laser power within 1.3 mm. With a spot diameter of 6.15 mm, this theoretically results in an ice disk with heat input, which only has a narrow edge strip where heat can be dissipated to the surrounding ice.

2. The ice is cooled by sublimation of the ice, as there is no external cooling system in the experimental setup. This means that the temperature of the ice surface is directly on the sublimation line according to the ambient pressure. Any energy input leads to sublimation and a temperature difference cannot be established. As a result, there is no temperature gradient in the experiments that could cause heat conduction.

The sublimation temperature $T_{\text{subl ice}}$ depends on the ambient pressure p. The mean value of the pressure that was measured for each drilling attempt was in the range of 80 Pa–250 Pa. According to equation (4), which is used to calculate the sublimation pressure of ice $p_{\text{subl ice}}$, this corresponds to sublimation temperatures of −62 °C to −53 °C.

$$p_{\text{subl ice}} = \exp\left(9.550426 - \frac{5723.265}{T_{\text{subl ice}}} + 3.53068 \ln\left(T_{\text{subl ice}}\right) - 0.00728332 \cdot T_{\text{subl ice}}\right) [40] \tag{4}$$

As a first approximation, an average sublimation temperature of −57.5 °C is used. Furthermore, the laser energy introduced is used to sublimate the ice, which achieves the desired drilling progress. The sublimation enthalpy h is also dependent on the ambient pressure. According to Feistel and Wagner [54] at the previously specified pressure (80 Pa–280 Pa) it reaches values of 2835 kJ/kg to 2837 kJ/kg [54]. At a sublimation temperature of −57.5 °C a sublimation enthalpy of 2836 kJ/kg is given. Lastly, the mass which has to be vaporized to generate the hole is determined by the volume of ice V vaporized per time unit t and its density ρ. The volume V can be calculated from the irradiated spot area A and the drilled depth, i.e. the drilling progress v_{drill}.

$$\frac{m}{t} = \frac{V}{t} \cdot \rho = A \cdot \frac{s}{t} \rho = A \cdot v_{\text{drill}} \cdot \rho \tag{5}$$

Based on this, the following equation can be used to calculate the drilling speed v_{drill}.

$$v_{\text{drill}} = \frac{(1-\eta) \cdot P_{\text{L}}}{\left(c_p \cdot \Delta T + h\right) \cdot \rho \cdot A} \tag{6}$$

Since the ice samples were stored in the freezer at approx. −20 °C before being measured, their temperature is above the sublimation temperature. During the evacuation process, ice evaporates and cools the ice surface down further. However, the ice that is not in contact with the vacuum continues to be warmed up by the ambient temperature. As a result, the energy required to raise the ice temperature to the sublimation temperature, as given in equation (6), can be neglected. The equation is therefore simplified as follows:

$$v_{\text{drill}} = \frac{(1-\eta) \cdot P_{\text{L}}}{h \cdot \rho \cdot A} \tag{7}$$

The fact that the ice temperature is close to the sublimation temperature means that no temperature gradients can arise due to the heating of ice, as it sublimates immediately instead of heating up when energy is introduced. Due to small to no temperature gradients, heat conduction in the ice is only very small or non-existent and is therefore neglected.

Various thermal models have been developed for simulating the progress of melting probes inside ice, starting with the one developed by Aamot [56]. The equation presented here is a simplified form of Aamot's melting equation, with the difference that the sublimation enthalpy is used and the reflection losses of the laser are taken into account as well. As shown below, the test results for clear ice samples and granular ice can be well recalculated. Applying equation (7) to dusty ice samples does not yield the correct drilling speeds (see Fig. 13). Assuming that only the sublimation of ice causes the drilling progress the mass of the dust can be neglected. This leads to the following equation:

$$\rho_{\text{real\_ice}} = \frac{m_{\text{probe}} \cdot (1 - \omega_{\text{dust}})}{V_{\text{probe}}} \tag{8}$$

As a result, the density of pure ice $\rho_{\text{real ice}}$ in the sample is significantly lower. Here, ω_{dust} is the dust fraction in the sample with the volume V_{probe} and the total weight m_{probe}. If this new ice density is used in equation (7), a good agreement can be achieved for dust mass fractions <90 wt% between calculated and measured drilling speeds.

3. Results

3.1. Clear ice and granular ice

Fig. 3 shows the drilling progress in clear ice at different laser powers. During the measurements, the laser rangefinder occasionally reported errors because the reflectivity of the drilling ground in clear ice is low. No depth could be determined for these errors. The 19.7 W curve was created using 3520 depth measurements, all of which were successful. For the 17 W curve, 60 depth measurements out of 8033 failed. For the 14.4 W curve, 74 out of 4434 depth measurements were not possible, and for the 8.8 W curve, 8 out of 4238 depth measurements failed. Fig. 4 shows a drilled ice sample. The conical drilling channel that results from the Gaussian intensity distribution in the laser spot is typical here. At the bottom of the sample is a ceramic plate that stops the drilling progress and protects the sample tube from being drilled through. The hole diameter on the surface was subsequently measured on the basis of photographs for some of the clear ice samples. This was on average 8.5 mm.

The drilling progress in granular ice could also be tracked during the drilling process. Various ice samples with a depth of 10.4–25 cm were drilled through completely or partially. Some samples were not perfectly aligned to the drilling laser, which is why they were drilled through diagonally with the channel hitting the wall of the sample tube. The mean drilling speed was therefore only determined using the available distance-time curve. The grain size varied from <0.1 mm to 5 mm. The bulk density of the granular ice samples ranged from 295 to 497 kg/m^3. Fig. 5 shows an example of the drilling progress in granular ice at different laser powers, densities and grain sizes. In contrast to the drilling in clear ice, there are almost no error outputs from the laser rangefinder in the recorded drilling progress. An average hole diameter on the surface of 7.6 mm was subsequently measured for some samples using photographs.

During the tests, it could be seen that the generated water vapor blows some ice particles out of the borehole. It was also observed that the particle flow from the borehole increased as the size of the ice grains used in the samples decreased. The particle flow was visible when the laser rangefinder irradiated the ice grains as they were blown out of the borehole, as shown in Fig. 6. The snapshots were taken for granular ice samples with different grain sizes.

3.2. Dusty ice

Ice samples with a dust mass fraction of 50–96.6 wt% were drilled. The bulk density of the ice-dust mixture varied between 494 and 1215 kg/m^3. Quartz, basalt, granite, bentonite, pumice, garnet and copper were used as additives, having densities mainly in the range of 2400–3950 kg/m^3, with copper extending the range to 8960 kg/m^3. The following Fig. 7 shows some samples during the drilling test inside the vacuum chamber.

It was observed that the dust is blown out of the borehole by the generated water vapor. Even copper particles with their high density of 8960 kg/m^3 were blown out of the borehole. The dust particles reached

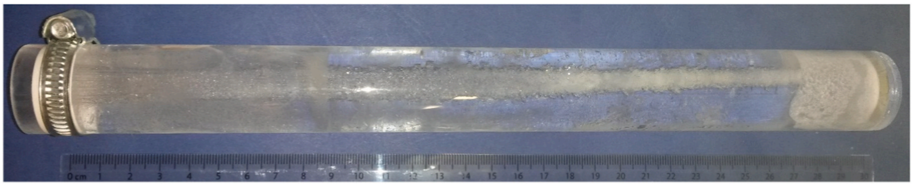

Fig. 4. Drilled clear ice sample.

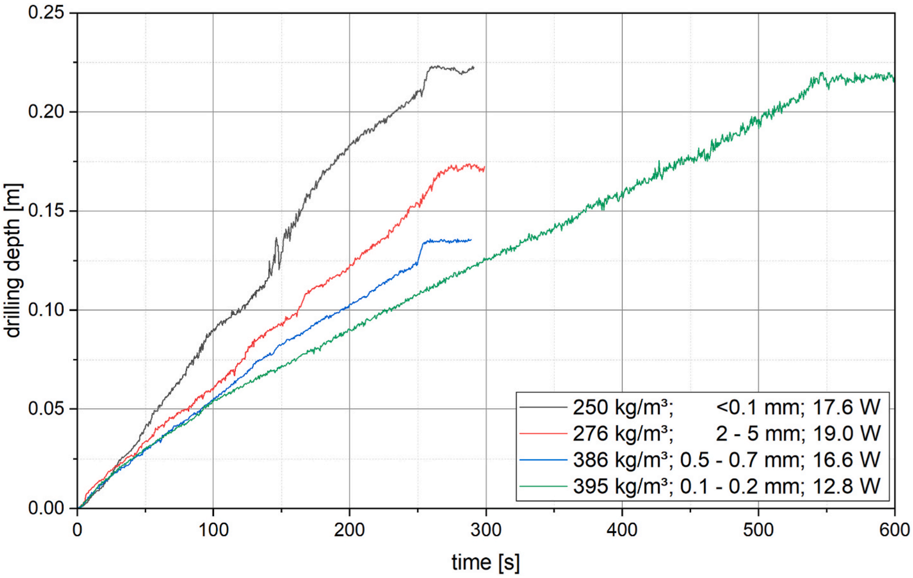

Fig. 5. Drilling depth plotted over time for various samples of granular ice with different heights. (For interpretation of the references to colour in this figure legend, the reader is referred to the Web version of this article.)

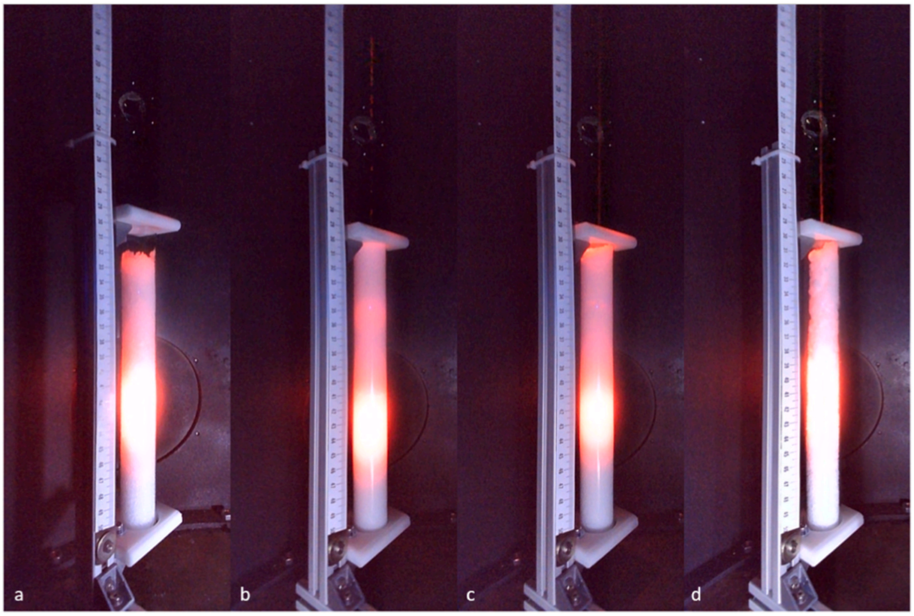

Fig. 6. Snapshots of the drilling attempt in samples with granular ice. Grain sizes: 2–5 mm (a), 0.33–0.5 mm (b), 0.1–0.2 mm (c), <0.1 mm (d). The current drilling depth can be identified by the laser rangefinder shining in the sample. Blown-out ice particles can be seen, which are illuminated by the laser rangefinder. The visible output of ice particles increases with decreasing grain size.

the deflection mirror and partially settled there (Fig. 8, left). The deflection mirror was located approx. 33 cm above the ice sample. Further dust particles were deflected by the deflection mirror in the direction of the vacuum chamber's viewing port and deposited in the flange socket in front of the viewing port (Fig. 8, right). The particle stream was partially illuminated by the laser rangefinder, which made it

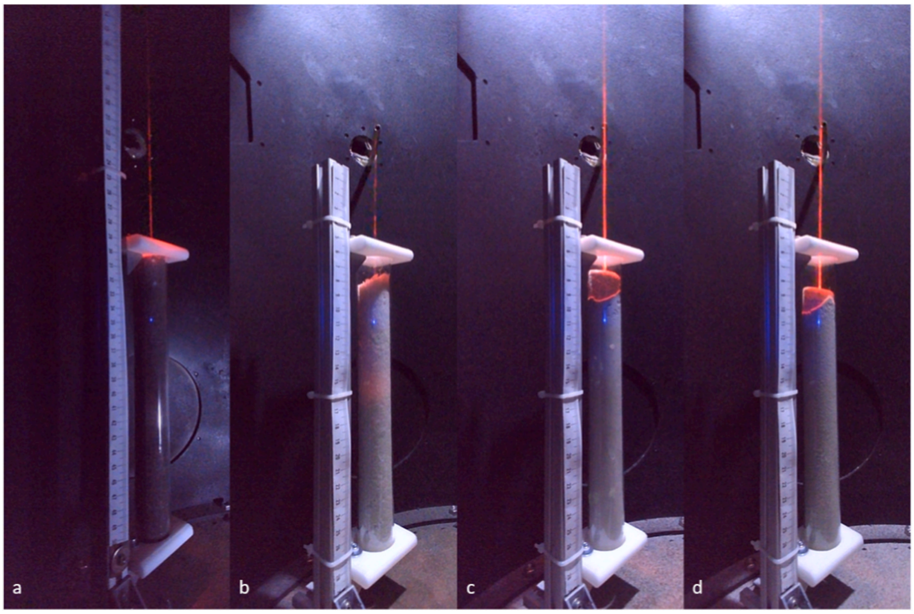

Fig. 7. Dust-ice samples during the drilling process: a: 50 wt% basalt ice mixture with <0.3 mm dust grain size, average laser power 2.34 W; b: 50 wt% quartz-ice mixture with 0.1–0.25 mm dust grain size, average laser power 10.6 W; c: 75 wt% quartz-ice mixture with 0.1–0.25 mm dust grain size, average laser power 9.6 W; d: 90 wt% quartz-ice mixture with 0.1–0.25 mm dust grain size, average laser power 10.3 W. The dust particles are blown out of the hole and illuminated by the laser rangefinder. The scattered light from the red laser rangefinder illuminates the surface of the sample and penetrates into the gap between the sample tube and the sample material. In the 50 wt% quartz-ice sample b, light shines through the sample material, giving an indication of the current drilling depth. (For interpretation of the references to colour in this figure legend, the reader is referred to the Web version of this article.)

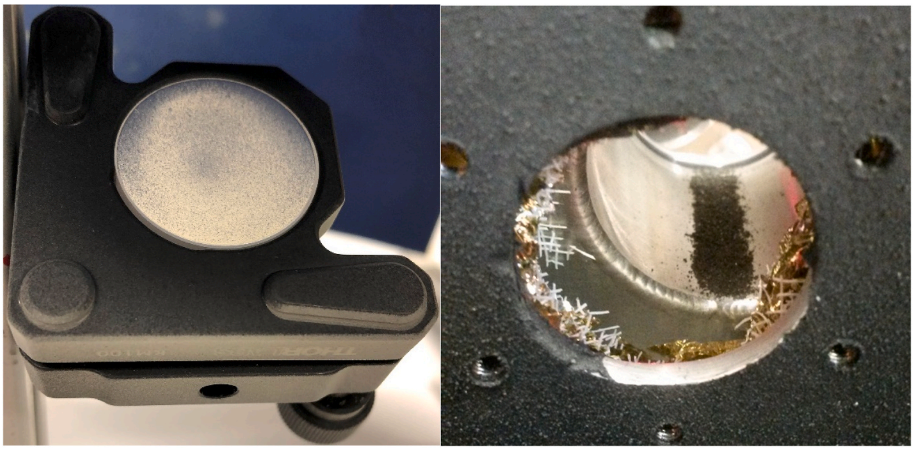

Fig. 8. Deflecting mirror contaminated with dust from drilling samples (left). Dust was deflected from the deflecting mirror into the flange socket of the laser viewing port (right).

visible (Fig. 7).

Tracking the drilling progress in dusty ice was not always successful. In particular, ice samples with small dust particles caused the deflection mirror to become covered with these particles, which meant that depth measurement was no longer possible. The dusty mirror also absorbed a part of the laser power required for the drilling process. Especially bentonite with a grain size <63 μm lead to a rapid contamination of the mirror and thus to a loss of depth measurement and a reduction in laser power. The mass fraction of dust in the ice played a minor role in the power loss. The drilling depth achieved was mainly independent of the dust fraction or dust grain size. However, the maximal drilling depth declined at a dust mass fraction of about 90 %. Only little progress could be made in the dust-ice mixture with a dust mass fraction of 96.6 %. It is assumed that the mixture was not sufficiently homogeneous, so that areas of pure dust were drilled into that could not be penetrated further. Poor mixing is also suspected in the 89 wt% bentonite dust-ice sample. Here, the laser did not penetrate the ice at all (Fig. 9a). An average hole diameter on the surface of 9.9 mm was subsequently measured for some samples using photographs.

Below, two basalt-ice samples and two quartz-ice samples were cut open after drilling. Their depth-time curves are shown in Fig. 10. All samples were drilled through, even though for some samples the depth measurement failed during the drilling process.

Fig. 11 shows an example of the drilling progress in dusty ice at different laser powers, dust content and grain sizes. During drilling in a 66 % basalt dust-ice mixture, the laser rangefinder determined the distance 709 times. In one attempt, the distance measurement was not successful. For drilling into a 50 % quartz dust-ice mixture, 1139 distance measurements were performed, of which 3.3 % were unsuccessful. These occurred most frequently in the range around 260 s, 420 s and 540 s, reaching moving average error rates of 20 %, 8.9 % and 8.9 % for over 100 measurements. The corresponding gaps are clearly visible in

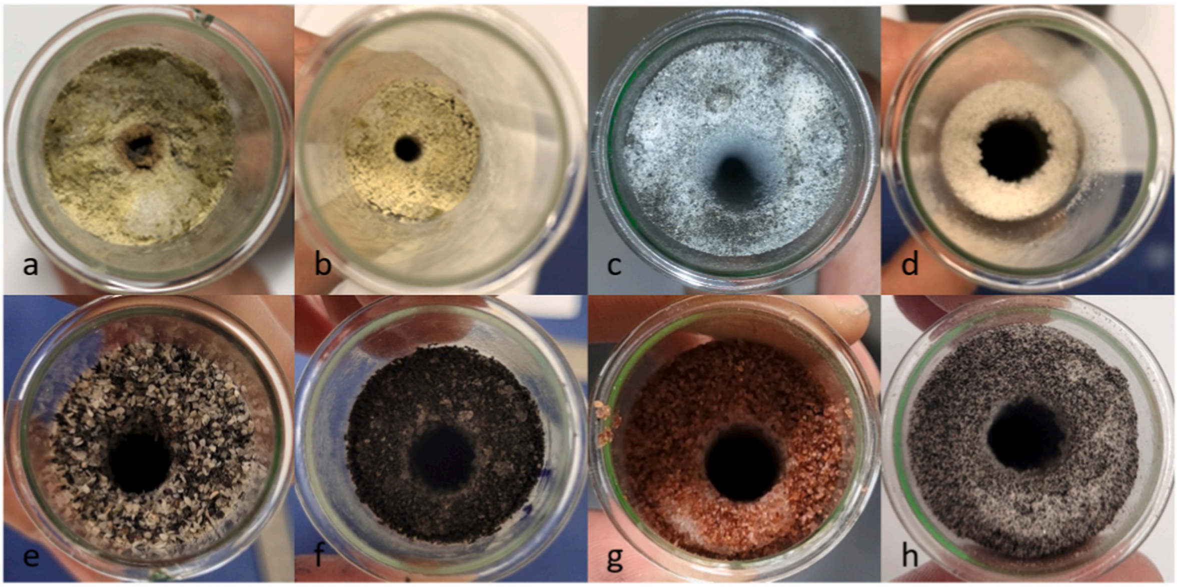

Fig. 9. Drill samples after the drilling attempt from above. a: 89 wt% bentonite-ice mixture, <0.063 mm dust grain size, <1 mm ice grain size; b: 78 wt% bentonite-ice mixture, <0.063 mm dust grain size, <1 mm ice grain size; c: 50 wt% basalt-ice mixture, <0.3 mm dust grain size, 0.5–0.77 mm ice grain size; d: 90 wt% quartz-ice mixture, 0.1–0.2 mm dust grain size, <1 mm ice grain size; e: 75 wt% granite-ice mixture, 0.5–1 mm dust grain size, 0.77 mm ice grain size; f: 75 wt% basalt-ice mixture, 0.1–0.6 mm dust grain size, 0.77 mm ice grain size; g: 75 wt% garnet-ice mixture, 0.4–0.8 mm dust grain size, 0.77 mm ice grain size; h: 75 wt% granite-ice mixture, 0.1–0.3 mm dust grain size, 0.77 mm ice grain size.

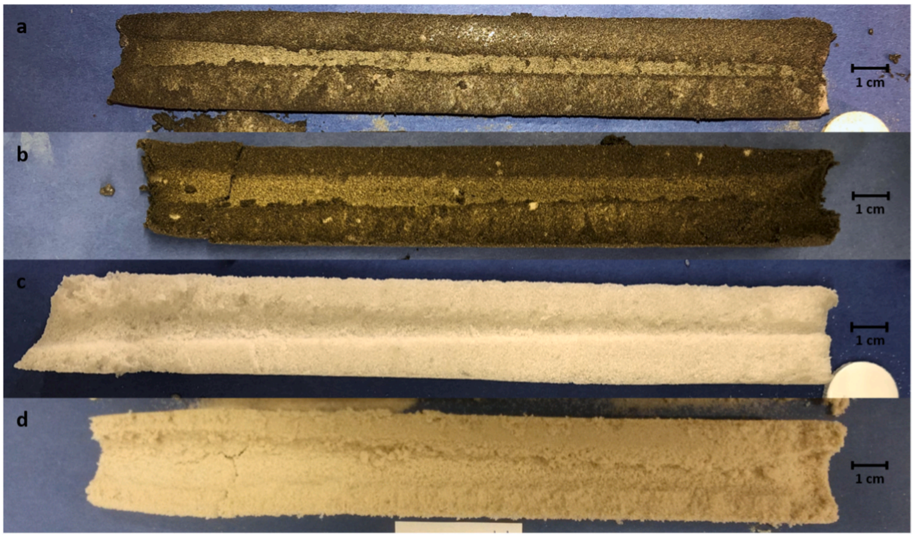

Fig. 10. Drilled and cut in half samples. a: basalt particles <0.3 mm; ice particles <1 mm; 66 wt% dust. b: basalt particles <0.3 mm; ice particles <1 mm; 75 wt% dust. c: quartz particles 0.1–0.25 mm; ice particles <1 mm; 50 wt% dust. d: quartz particles 0.1–0.25 mm; ice particles <1 mm; 90 wt% dust. The samples were drilled from the left-hand side. Accordingly, a conical shape of the drill channel can be recognized. At the lower end of the samples, the ceramic plates that protected every sample tube can still be partially seen in a and c. If the drilling laser was still switched on after the entire sample had been drilled through, the ceramic plate reflected the laser beam diffusely upwards, causing the channel to widen, starting from the bottom. This can be seen in b and d.

the diagram. The drilling into a 90 % quartz-ice mixture was tracked with 830 measurement attempts. 47 % were successful. Starting at 150 s, the error rate in the moving average of 100 measurement attempts rises from 0 % to 100 % and then falls to a local minimum of 66 % at 300 s. The drilling in a 75 % basalt-ice mixture was tracked with 1249 measurement points. Up to 130 s, the error rate is 2 %. Subsequently, it rises to 100 %.

3.3. Measurement results and comparison with the thermal model

The following Fig. 12 shows the average drilling speeds of all drillings in clear ice, granular ice and dusty ice over the average laser power. As can be seen, the average drilling speed increased with the laser power. Higher drilling speeds were also achieved in samples with granular ice than in samples with clear ice. This is due to the lower density of the ice bulk, which means that less energy is required to sublimate a certain volume of ice. The drilling progress in dusty ice samples was even faster than that of granular ice, although the total sample densities were higher than those of clear ice due to the sometimes quite high dust fraction. Furthermore, the drilling speeds for ice according to the thermal model in equation (7) are illustrated. The reflectivity used in the thermal model of the ice varies between 0 % and 10 %. In the thermal model, a mean density of 918 kg/m^3 for clear ice and a mean bulk density of 433 kg/m^3 for granular ice was used. The

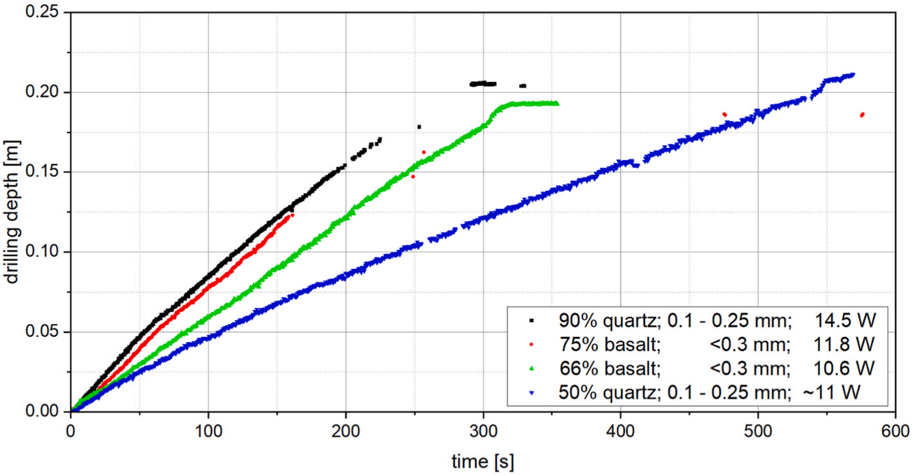

Fig. 11. Depth-time diagram recorded with the laser rangefinder for two basalt-ice and quartz-ice mixtures. Gaps in the path-time curve show that the laser rangefinder was no longer able to determine the depth correctly due to the mirror contamination. Instead, the laser rangefinder returned error values or the distance to the mirror. (For interpretation of the references to colour in this figure legend, the reader is referred to the Web version of this article.)

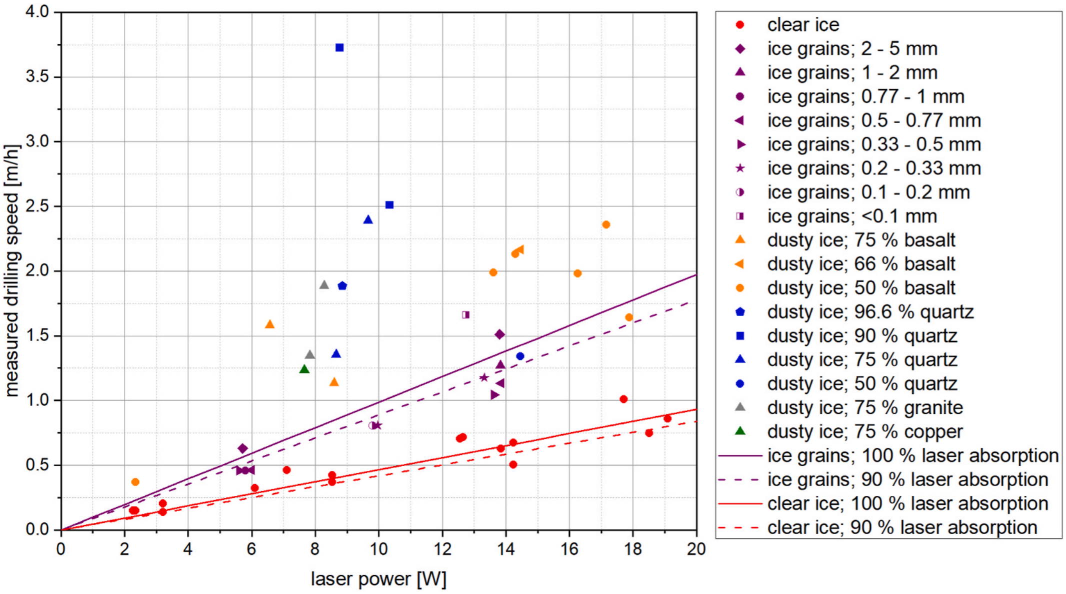

Fig. 12. Average drilling speeds determined with a laser rangefinder in clear ice, ice with different grain sizes and ice with different dust mixtures. The lines show the drilling speeds predicted by the thermal model from equation (7) at 100 % and 90 % laser absorption in clear ice with a density of 918 kg/m^3 and granular ice with a bulk density of 433 kg/m^3. (For interpretation of the references to colour in this figure legend, the reader is referred to the Web version of this article.)

measured bulk densities of the ice samples with granular ice, on the other hand, ranged from 295 to 497 kg/m^3.

If the density of each sample and the respective mean laser power are used to calculate the respective drilling speed and this is then plotted against measured drilling speed, the following Fig. 13 is obtained. For clear ice, a surface reflectivity of 1.65 % was chosen, and for granular ice and dusty ice a reflectivity of 8.5 %. For the clear ice samples and the granular ice samples, the drilling speeds can be well adjusted with the theoretical model for ice close to the sublimation temperature (equation (7)). The sublimation enthalpy was determined based on the average pressure, which was recorded over the entire drilling process. The drilling speed in dusty ice samples could not be determined with this approach. In the case of the dusty ice samples, only samples were selected whose hole progress could be tracked at least to a depth of 78 % of the sample depth. Furthermore, one drilling attempt was rejected due to strong inhomogeneities in the ice-dust distribution; another was rejected due to extremely fluctuating depth measurements.

The following diagram (Fig. 14) shows those drilling speeds. Here, the density of the dusty samples was adjusted according to equation (8) and calculated according to equation (7). This means that a large part of the results of the dusty samples can now also be modeled to a good approximation. As before, only samples were considered which could be tracked with the laser rangefinder to a drilling depth of at least 78 % of its sample length, showed no relevant inhomogeneities in the mixture and no strong fluctuations in the distance measurement. The deviating data point at 2.5 m/h measured drilling speed/4.1 m/h calculated drilling speed belongs to a 90 % quartz-ice sample with 0.1–0.25 mm dust grain size. Due to the heavily contaminated deflection mirror, only an average of 10.3 W of the original 20 W laser power reached this sample for drilling. The drilling velocity of another 90 wt% quartz-ice sample with a dust grain size of 0.1–0.6 mm was measured at 3.73 m/h and calculated at 3.68 m/h. A clean mirror was used here, which meant that 8.8 W of the 10 W emitted were available for the drilling process and used in equation (7).

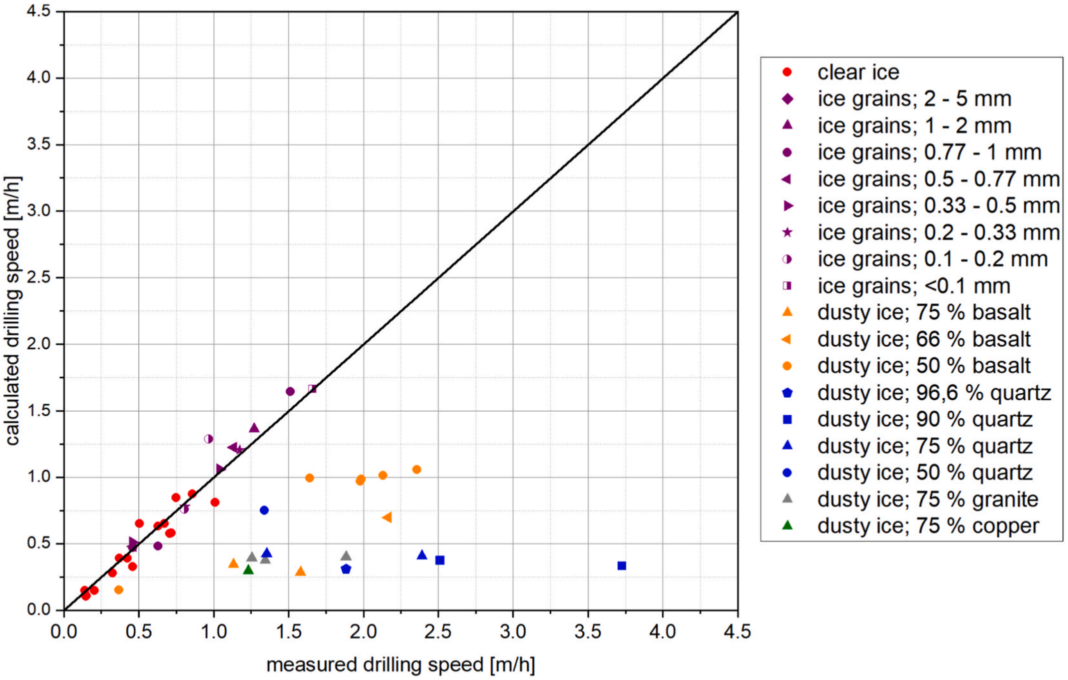

Fig. 13. Calculated drilling speed according to equation (7) plotted against the measured drilling speed. Drilling speeds of clear ice samples, granular ice samples and dusty ice samples are shown. (For interpretation of the references to colour in this figure legend, the reader is referred to the Web version of this article.)

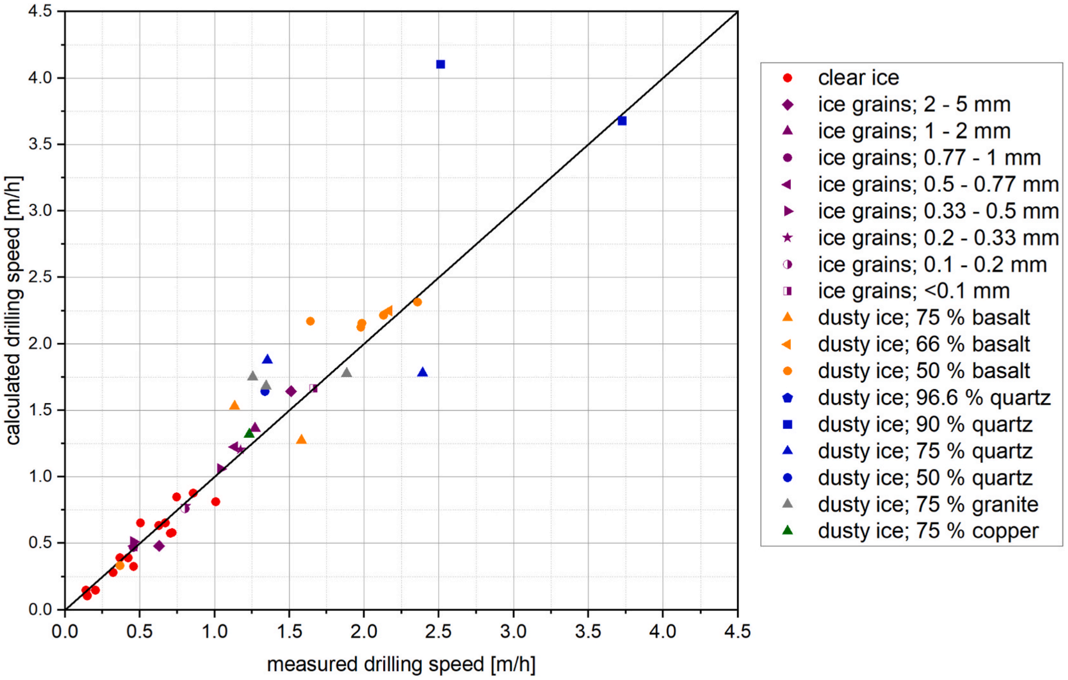

Fig. 14. Calculated drilling speed according to equation (7) plotted against the measured drilling speed. Drilling speeds of clear ice samples, granular ice samples and dusty ice samples are shown. The drilling speed of the dusty ice samples was calculated using the pure ice density of the samples (equation (8)). (For interpretation of the references to colour in this figure legend, the reader is referred to the Web version of this article.)

4. Discussion

4.1. General measurement errors

Every parameter in equation (7) (drilling speed, sample density, reflectivity) is prone to measurement errors. Possible reasons for errors in determining the speed are imperfect alignment of the two laser beams and a contamination of the deflection mirror. Furthermore, other processes not taken into account, such as laser scattering due to dust flow or the blowing out of ice grains, can influence the drilling process.

4.1.1. Imperfect alignment

For optimal accuracy the beams of the drilling laser and the range-finder have to be aligned perfectly collinear. As the power distribution in the beam of the drilling laser is Gaussian the resulting channel has a slight conical form. Therefore, even a slight deviation in the alignment can lead to underestimating the drilling speed, since the rangefinder does not reach the true bottom of the drilling hole, but hits the side wall of the drilling hole. We estimate that drilling speed errors of up to −15 % can occur here.

4.1.2. *Contamination of the mirror*

In the thermal model an average laser power is used. This is calculated from measurements of the laser power taken before and after each drilling. If there is early contamination of the mirror, leading to an early loss of laser power, the calculated drilling speed will be higher than the real one. Late dusting of the mirror has the reverse effect. This leads to an estimated error in the range of ±20 %. The different reasons for the contamination are as follows.

Occasionally, material in the form of water droplets, which are ejected from the clear ice samples, reaches the deflecting mirror and thus reduces its reflectivity.

In the case of granular ice samples, it was observed that ice particles were blown out of the hole by the water vapor generated at the bottom of the hole. The smaller the ice particles used, the more ice particles were blown out of the borehole (see Fig. 6). Demineralized water was used to produce the ice. However, this still contains some impurities that remain on the mirror surface when the ice grain or water droplet is sublimated or vaporized by the drilling laser shining on the mirror.

In the case of dusty samples, the dust is driven out of the hole during the drilling process and thrown against the deflection mirror above the drill sample. This causes the mirror to be sandblasted to a certain extent, which reduces its reflectivity (see Fig. 8). However, its reflectivity also decreases because particularly small dust particles adhere to the mirror.

4.1.3. *Sample density*

The density is necessary to calculate the theoretical drilling speed. The density itself is calculated using measurements of the sample volume and its weight. The sample diameter could be determined fairly accurately whereas errors determining the sample height could occur. On the one hand the surface of the sample is not completely flat, on the other hand the ceramic plate at the bottom, which is used to protect the sample container from the laser, creates a cavity. This is taken into account for the calculations. But small amounts of ice could accumulate below the ceramic plate during the filling procedure leading to a higher weight but not contributing to the sample mass and thus falsely increasing the density. We estimate that the error in determining the reference density is in the range of 2 %–6 %.

Furthermore, higher melting velocities than theoretically possible can be achieved in clear ice samples because the ice was not completely free of air bubbles. We estimate that this can reduce the density measured with the laser drill by up to 6 %.

In dusty ice samples, an inhomogeneous mixture could lead to more ice or more dust being drilled than determined by the mean value, so that the actual drilling speed deviates from the theoretical value. The sample tubes have a diameter of 28 mm and the drilling laser has a diameter of 6.15 mm. This means that the laser can only sublimate approx. 5 % of the sample for density determination. The overall composition of the sample is not fully captured by the drilling laser. Inhomogeneities that lie outside this zone can therefore not be taken into account. This effect is exacerbated if a sample could not be completely drilled through. In this case, local inhomogeneities that have a higher density, for example, and increase the overall density of the sample would not be detected by the laser drill and therefore contribute to a lower density determination. The samples were only not drilled through completely if the deflection mirror became so clogged with dust that depth measurement was no longer possible. In this case, the drilling process was aborted. We estimate that the inhomogeneities account for an error of ±5 %.

4.1.4. *Ice reflectivity*

The reflectivity determines how much laser power is available for the drilling process. However, this value varies depending on the grain size of the bulk material [55]. The reflectivity of the dust sample is influenced by the dust fraction. As only the ice content is sublimated, only its reflectivity was considered. In both cases, a reflectivity of 8.5 % was assumed. We estimate that the error in the correct laser reflection determination is in the range of −8.5 %–50 %.

4.1.5. *Other not considered drilling processes*

Higher melting rates than calculated can also occur if the drilling process is supported by blowing the ice and dust grains out of the borehole. In this case, the particles are not removed by sublimation, but by blowing them away, for which no laser power is required. The extended thermal model shows that this effect must be taken into account, at least for dusty ice samples, which is why only the pure ice density of the dusty samples is used for the calculations.

In dusty ice, a stream of dust moves towards the mirror while drilling. This leads to scattering of the laser light, which further hinders the drilling process and reduce the drilling speed. We estimate that up to 5 % of the laser light is lost due to the scattering process in the laboratory tests.

The pressures were measured at the lid of the vacuum chamber. The real pressure at the bottom of the borehole could have been higher and could have increased further with the progression of the borehole, since this long thin channel might represent a certain flow resistance to the water vapor. Accordingly, the sublimation enthalpy also changes in a range from 0 to 1 %. In the case of dusty ice samples, the additives can absorb laser energy while they are lying on the ground and carry it with them when they are blown out. This effect is estimated to be very small, as the heat capacity of ice is at least twice as large as that of the additives. As a result, the additives heat up faster than the ice at the same laser irradiation. However, this creates a temperature gradient that causes a heat flow in the direction of the surrounding ice. In addition, as soon as this ice, which is close to the sublimation point, is sublimated, the adjacent dust particle is also blown out by the water vapor.

4.2. *Effects of uncertainties on the overall measurement result*

Not all measurement errors occur at all ice types, and even if they do occur, they are not always equally pronounced. Overall, a measurement uncertainty of ±5 % is assumed for the determination of the laser spot area. The total uncertainty is determined for all subsequent measurement uncertainties according to Gaussian error propagation. The calculated speed based on the measured ice density is subject to a relative uncertainty of ±13 % for clear ice. For granular ice samples, the relative uncertainty is ±16 % and for dusty ice samples ±56 %. This is also clearly reflected in the distribution of data points in Fig. 14. The measurement points for clear ice samples and granular ice samples are much closer to the diagonal than the measurement points for granular ice samples. The measurement point (2.5 m/h, 4.1 m/h) is even higher than the calculated relative uncertainty at 64 %. The determination of the drilling speed is relevant for mission planning. Here it can be used to establish time and energy budgets for reaching specific drilling depths. The relative uncertainty for density is relevant for measurements on a celestial body. This is because the drilling speed can be used to create a depth-resolved density profile of the drilled ice layer. Due to the high measurement frequency and slow drilling speed, the depth resolution is in the millimeter range. According to Gaussian error propagation, the relative uncertainty for density determination is ±19 % for clear ice and granular ice and ±57 % for dusty ice. Perfect alignment of the drilling laser and distance lasers can minimize the relative error to ±11 % for clear ice and granular ice. If the degree of reflection is also determined perfectly before and during drilling, the density of all ice types can be determined with a relative uncertainty of ±7 %.

4.3. Possible applications of a laser ice drill

A combination of laser drill and rangefinder as presented here, in conjunction with gas analysis and dust analysis systems (see Fig. 15), could be a possible payload for lander missions to icy celestial bodies. The composition of the gas at the borehole outlet could be analysed using a mass spectrometer or a cavity ring down spectrometer, for example. Non-volatile particles could be filtered out of the water vapor stream using an electrostatic separation process (see Fig. 15) to protect the laser optics and collect the dust for further analysis. This could involve drilling into dusty ice at set depth intervals. The dust from each depth section is collected and immediately analysed or filled into sample tubes for later analysis on site or on Earth. This technique could also be used on a comet mission. Drilling into comet nuclei seems possible because nuclei consist of a mixture of solids and frozen volatiles. For example, 75 % [57] of the mass of Comet Halley consists of non-evaporable material, while the rest is water or other volatile substances such as CO_2 or CO [58]. Choukroun et al. gives a refractory to ice mass ratio of 3:1 or greater for the comet nucleus of 67P/Churyumov--Gerasimenko [59]. This corresponds to a dust mass fraction of 75 % or greater in the experiments carried out in this study. Pätzold et al. gives an upper limit of 7:1, which corresponds to a 87.5 % dust mass fraction [60].

Since the presented experiments successfully drilled through ice with a dust mass fraction of at least 90 %, the use on comets seems possible. If no layers without ice are present, the entire cometary nucleus could theoretically be drilled through and a complete cross-section of the dust and ice properties of the comet's nucleus could be obtained. The only limitation in this case appears to be the beam expansion of the drilling laser and the associated decrease in the drilling progress.

Drilling into permanently shaded lunar craters could also be possible. For example, Luchsinger et al. [61] determined a water ice mass fraction of 8.2 % in Cabeus crater. While the spectral modelling Li et al. [62] shows that ice mass fractions of up to 30 % may be present in some lunar craters.

With regard to the water content in the Martian soil, drilling appears to be possible at higher latitudes, as water contents of up to 13 % have been estimated from orbital near-infrared reflectance spectra [63]. At the landing site of the Phoenix lander, pore ice with a proportion of 30 ± 20 % by weight was detected during digging, which was trapped between the grains of the soil [64]. However, since the average surface pressure of 610 Pa [46] is at the triple point of water, depending on the actual ambient pressure at the drilling site, meltwater could also be produced instead of a steady water vapor and particle stream. The southern plateaus, where the surface pressure is between 82 and 480 Pa [65], are more preferable in this case.

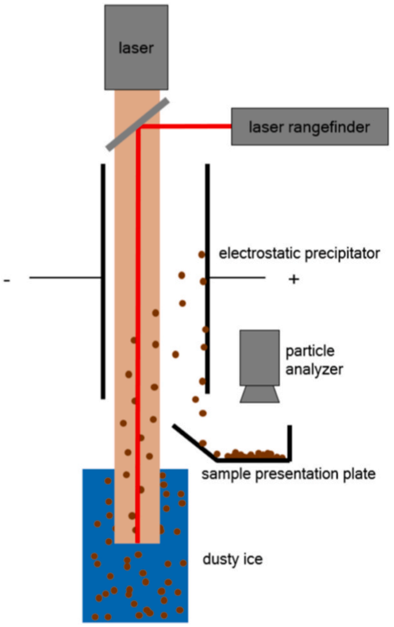

Fig. 15. Possible laser ice drill configuration with electrostatic dust filter to protect the laser optics and to collect and analyse dust samples.

However, ice layers with less dust, such as the polar caps of Mars, Pluto or icy moons such as Enceladus or Europa, can be easily drilled into. Here it is possible to detect the additives at a specific depth and the density of the ice by calculating a density profile from the measured drilling speed using equation (7). An exception to this is Saturn's moon Titan, whose surface pressure of 1.5E5 Pa is far too high for a sublimation process [66].

4.4. Deep drilling

In the first experiments on laser drilling in granular ice and dusty ice presented here, maximum drilling depths of 25 cm were achieved. If the ice cover of an icy moon is to be examined or a comet nucleus drilled through, holes several kilometers deep must be drilled. This raises the question of whether the drilling progress observed here can be maintained in the long term. This will most likely not be the case, as the following mechanisms, which only come into play at greater depths, counteract the drilling progress.

A first mechanism is the pressure build-up in the borehole due to the constant laser-induced sublimation. Due to the pressure gradient between the sublimation front and the vacuum above the borehole exit, the generated water vapor can flow out. The longer the ice channel through which the water vapor flows, the greater the flow resistance. This causes pressure to build up at the bottom of the borehole, which increases the sublimation temperature further and further. As a result, the ice must be heated far above the ambient temperature until sublimation occurs. In extreme cases, the pressure can exceed the triple point of the ice. Melt water would then form at the bottom of the borehole, absorbing the laser power and using its energy to melt the ice evenly in all spatial directions. No more material would be extracted from the borehole, which would end the progress of the borehole. Excessive pressure build-up could be avoided by drilling only at intervals from a certain depth. The pause times would serve to give the gas time to flow out of the hole and reduce the pressure gradient between the bottom of the hole and the outlet. This method would save a lot of laser power, but would considerably delay the drilling process.

Another possible mechanism is the clogging of the borehole channel with ice. It is assumed that the water vapor cools down as it rises in the hole and partially resublimates on the hole wall before escaping. As long as the drilling laser is in operation, the borehole channel is flooded with laser light. Every deposit at the edge of the borehole, which is presumably only as large as the diameter of the drilling laser, is illuminated by it and sublimates again. This would cause laser energy to be applied that should actually be used to advance the hole. This would slow down the progress of the hole at the edge of the hole and the drill hole would become more and more pointy. The generated water vapor, on the other hand, can also be so hot that it melts the drill hole beyond the laser diameter. In this case, too much energy would be absorbed during the sublimation process, which is a sign of an inefficient drilling process. Random measurements have shown that the exit holes in the clear ice samples have an average diameter of 8.5 mm, the granular ice samples have an average diameter of 7.7 mm and the dusty ice samples have an average diameter of 9.9 mm. As the laser spot diameter was only 6.15 mm, this could be an indication that the borehole was widened by the rising water vapor.

Furthermore, from a certain depth, the borehole will be closed by the pressure of the ice above it. On earth, boreholes can be drilled to depths of 300–350 m without drilling fluid, which keeps the borehole open. The ice temperature, drilling speed and permissible borehole alteration also play an important role here. Talalay et al. [67] simulated that borehole depths of 230 m can be achieved with a maximum borehole constriction of 0.5 mm at ice temperatures of −20 °C on earth. If the ice is −50 °C cold, almost 500 m can be reached. However, due to the low gravity of the icy moons and the even lower temperatures, much greater drilling depths should be achieved before the inflow of the borehole becomes a problem. Cardell et al. [31] predicts that a 3 km borehole is possible without inflow from the Martian polar ice caps.

The surface temperatures on the icy moons are close to the sublimation temperature. Nevertheless, this can be considerably lower in areas not exposed to the sun. Here, the ice must first be heated up to sublimation temperature with the laser before it sublimates. Accordingly, heat losses can occur that reduce the efficiency of the drilling process. According to the heat capacity of the ice, heating the ice by 100 K would amount to around 7 % of the sublimation enthalpy. With regard to heat conduction losses, reference should be made to the work of Ulamec et al. [68], who determined the drilling efficiency of melting probes as a function of melting speed and ice temperature. Schüller and Kowalski [69] determined the efficiency as a function of the melting probe length. In order to be able to apply the results to the laser ice drill, it can be regarded as an extremely short melting probe as a first approximation. Accordingly, the losses are considerably lower than with conventional melting probes. Whereas with a melting probe the melting head and the jacket conduct the heat into the surrounding ice, with a laser it is only emitted through a small, narrow laser-irradiated zone similar to the melting head.

4.4.1. *Initial considerations for a possible mission*

The testing of drilling very deep holes could initially be carried out in the Arctic or on a glacier. While it is possible to drill vertically in Antarctica and thus demonstrate drilling to very great depths, only shallow drilling depths can be demonstrated in glaciers. Here, drilling parallel to the glacier surface could promise longer boreholes. At both demonstration sites, however, a vacuum bell must be used, which is rammed into the ice with the open side facing down. This can then be used to create a vacuum of about 1 mbar, which is necessary for the laser drilling process described here. If a crevice is drilled into a glacier, air can enter the borehole, causing the vacuum to collapse. This must be prevented by appropriate drilling direction planning.

When using the laser drill on icy moons, the areas where the ice is warmest should be used. This can save a few percent, which would otherwise have been needed to heat the ice to sublimation temperature.

For drilling ice in permanently shaded craters on the Moon and Mercury, a lander with a laser drill can land there and take direct gas and dust samples from the borehole. However, alternative solutions to solar cells must then be used to ensure a power supply. Landing the lander on the crater rim offers the possibility of supplying the lander with power via solar cells. The laser drill can be aimed at a point in the crater over a long distance and drill a hole there. However, the laser beam widens slightly until it reaches the crater bed, which means that the maximum laser intensity and thus drilling speed cannot be achieved. Furthermore, remote sensing methods must be used to analyse the hole ejecta from the crater rim.

When drilling into dusty ice, care must be taken not to drill into a layer that is free of ice. If the top layer is free of ice, it can be overcome or removed using conventional drills for thicker layers or brushes or blowing systems for very thin layers of dust.

In experiments, dusty ice with a grain size of up to 1 mm was successfully drilled. Whether larger dust particles can be ejected from the borehole has not been tested. For safety reasons, a landing site should be sought where the grain size of the dust is ≤ 1 mm. Non-evaporable obstacles larger than the laser beam diameter are not blown out of the borehole. These heat up and cause the surrounding ice to evaporate. As a result, stones sink further and further into the depths. Gas continues to rise to the surface and can be analysed. Whether dust lying beneath the stone can be transported out was not tested. The stone reduces the drilling speed according to its size. Overall, drilling into stones should be avoided, which is why preliminary exploration of the subsoil with radar instruments, for example, is recommended.

If water-bearing gaps are drilled into, the water inside them is vaporized until it is exhausted. The drilling process is then continued at the lower end of the gap. Drilling into gaps may be desirable if the entire contents of the gap are to be examined. However, if the gap contains too much water to be vaporized, the drilling process ends at this point. If the laser ice drill encounters liquid water, depth measurement is not possible. In this case, only the last depth measurement before reaching the gap can be used as an indicator of the gap's position. Once all liquid water has evaporated, distance measurements can be taken again and the width of the gap at the drilled location can be measured.

Tables 4 and 5 below summarise some parameters of a possible laser ice drill payload. The performance data is based on equation (7). The hardware data is based on a preliminary design draft derived from the laboratory equipment used and lasers of similar power. The specifications for the dust separation system, consisting of two 1 m long condenser plates and a high-voltage system, are based on design calculations that should lead to the acquisition of such a system. Since the laser drill is only suitable for determining density and lifting sample material, the Philae lander's Ptoloemy mass spectrometer/gas chromatograph is listed as a reference system for analysing gas additives. The Perseverance rover's PIXL alpha particle X-ray spectrometer is listed as the reference system for dust analysis. A dust separation system and devices for analysing the dust are only required when drilling dust-containing ice, which significantly reduces the mass for a possible mission to an ice moon compared to a mission to a comet or lunar crater.

5. Conclusion

A new method for drilling into celestial bodies was presented. The drilling tests with samples of clear ice, granular ice and dusty ice in the laboratory setup have met our first expectations. The results showed that a large number of celestial bodies can be drilled into as long as there is some ice in the ground and the pressure is below the triple point. The drilling speed is directly proportional to the laser power and indirectly proportional to the ice density. Accordingly, the drilling speeds increase with increasing dust content. A system derived from the laboratory setup is suitable for determining the depth-resolved ice density in an energy-efficient manner. Furthermore, the measurement results indicate that dust samples and water vapor samples could be lifted from the depth with this system for further analysis.

In order to clarify questions of borehole stability, deep borehole drilling or simulations would have to be carried out. Tests in the cryo-vacuum chamber can provide indications of possible heat conduction losses that could occur when drilling below the sublimation line.

For robust use on celestial bodies, proper dust separation should be implemented to allow proper dust sample analysis and, more importantly, to protect the laser optics from contamination.

Table 4
Preliminary data for a possible laser ice drill.

instrument	mass	volume	power requirement	destination
Laser ice drill	4 kg	15 x 20 × 15 cm^3	150 W	Icy moons, Pluto, polar caps on Mars, comets, ice-filled craters on the moon and Mercury
Ptolemy [70]	4.5 kg	25 x 33 × 11 cm^3	10 W	
electrostatic dust separation	6 kg	25 x 15 × 130 cm^3	100 W	Comets, ice-filled craters on the moon and Mercury
PIXL [71]	10 kg	21.5 x 27 × 23 cm^3	25 W	

Table 5
Performance of a possible 20 W laser ice drill, based on measurements of the here presented study. The laser aperture is 6.15 mm and the full divergence angle of the laser beam is 0.327 mrad.

Drilling speed in clear ice	$\leq$0.9 m/h
Drilling speed in granular ice with 500 kg/m^3	$\leq$1.6 m/h
Drilling speed in granular ice with 300 kg/m^3	$\leq$2.6 m/h
Drilling speed in dusty ice with 50 % dust mass fraction and a total density of 500 kg/m^3	$\leq$3.1 m/h
Maximum possible dust content in ice	90 %
Maximum possible dust particle size tested in ice	1 mm
Obstacles that should be avoided	Water-bearing gaps, stones, layers of dust with ice content <10 %

CRediT authorship contribution statement

Martin Koßagk: Writing – original draft, Visualization, Validation, Software, Project administration, Methodology, Investigation, Funding acquisition, Formal analysis, Data curation, Conceptualization. **Leo Peiffer:** Writing – review & editing, Data curation. **Lukas Mohr:** Writing – review & editing, Data curation. **Martin Tajmar:** Supervision. **Tino Schmiel:** Writing – review & editing, Supervision, Funding acquisition.

Declaration of competing interest

The authors declare that they have no known competing financial interests or personal relationships that could have appeared to influence the work reported in this paper.

Acknowledgements

We gratefully acknowledge the support for EnEx-EislaboHr by the German National Space Agency DLR (Deutsches Zentrum fuer Luft-und Raumfahrttechnik) by funding from the Federal Ministry of Economic Affairs and Energy (BMWi) by approval from German Parliament (50RK1953). Open Access funding enabled and organized by Projekt DEAL.

Appendix A. Supplementary data

Supplementary data to this article can be found online at https://doi.org/10.1016/j.actaastro.2025.08.049.

References

[1] W.A. Ambrose, The Significance of Lunar Water Ice and Other Mineral Resources for Rocket Propellants and Human Settlement of the Moon, AAPG Mem, 2013, https://doi.org/10.1306/13361567M1013540.

[2] K. Zacny, P. Metzger, K. Luczek, J. Mantovani, R. Mueller, The world is not enough (WINE): harvesting local resources for eternal exploration of space, in: AIAA Sp. Astronaut. Forum Expo, 2016, 2016, https://doi.org/10.2514/6.2016-5279. Sp.

[3] K.R. Erickson, Optimal architecture for an asteroid mining mission: equipment details and integration, in: Collect. Tech. Pap. - Sp. 2006 Conf, 2006, https://doi.org/10.2514/6.2006-7504.

[4] A.G. Marusiak, S. Vance, M.P. Panning, M. Behounková, P.K. Byrne, G. Choblet, M. M. Daswani, K. Hughson, B. Journaux, A.H. Lobo, B.E. Schmidt, K.P. Sládková, K. M. Soderlund, W.Z. Song, O. Souček, G. Steinbrügge, A.F. Thompson, S. Wang, Exploration of icy ocean worlds using geophysical approaches, Planet. Sci. J. 2 (2021), https://doi.org/10.3847/PSJ/ac1272.

[5] M. Wirtz, M. Hildebrandt, IceShuttle teredo: an ice-penetrating robotic system to transport an exploration auv into the ocean of Jupiter's moon Europa, in: Proc. Int. Astronaut. Congr., IAC, 2016.

[6] W. Stone, B. Hogan, V. Siegel, J. Harman, C. Flesher, E. Clark, O. Pradhan, A. Gasiewski, S. Howe, T. Howe, Project VALKYRIE: laser-powered cryobots and other methods for penetrating deep ice on ocean worlds, in: Outer Sol. Syst. Prospect. Energy Mater. Resour., 2018, https://doi.org/10.1007/978-3-319-73845-1_4.

[7] W. Zimmerman, R. Bonitz, J. Feldman, Cryobot: an ice penetrating robotic vehicle for Mars and Europa, in: IEEE Aerosp, . Conf. Proc., 2001, https://doi.org/10.1109/aero.2001.931722.

[8] J.A. Mikucki, C.G. Schuler, I. Digel, J. Kowalski, M.J. Tuttle, M. Chua, R. Davis, A. M. Purcell, D. Ghosh, G. Francke, M. Feldmann, C. Espe, D. Heinen, B. Dachwald, J. Clemens, W.B. Lyons, S. Tulaczyk, Field-based planetary protection operations for melt probes: validation of clean access into the blood falls, Antarctica, englacial ecosystem, Astrobiology 23 (2023), https://doi.org/10.1089/ast.2021.0102.

[9] C.R. Bentley, B.R. Koci, L.J.M. Augustin, R.J. Bolsey, J.A. Green, J.D. Kyne, D. A. Lebar, W.P. Mason, A.J. Shturmakov, H.F. Engelhardt, W.D. Harrison, M. H. Hecht, V. Zagorodnov, Ice drilling and coring, in: Drill. Extrem. Environ. Penetration Sampl. Earth Other Planets, 2009, https://doi.org/10.1002/9783527626625.ch4.

[10] Y. Sun, B. Li, X. Fan, Y. Li, G. Li, H. Yu, H. Li, D. Wang, N. Zhang, D. Gong, R. Wang, Y. Li, P.G. Talalay, Brief communication: new sonde to unravel the mystery of polar subglacial Lakes, Cryosphere 17 (2023) 1089–1095, https://doi.org/10.5194/TC-17-1089-2023.

[11] D.P. Winebrenner, W.T. Elam, P.M.S. Kintner, S. Tyler, J.S. Selker, Clean, Logistically Light Access to Explore the Closest Places on Earth to Europa and Enceladus, AGU Fall Meet. Abstr., 2016.

[12] W.C. Stone, V. Siegel, K. Richmond, J. Ralston, Deep Cryogenic Vacuum-Ice Testing of Cryobots: Project PROMETHEUS, IEEE Aerosp. Conf. Proc., 2023, https://doi.org/10.1109/AERO55745.2023.10115645.

[13] V. Guerrero, W. Stone, V. Siegel, B. Hogan, K. Richmond, J. Harman, K. Myers, S. Lelievre, C. Flesher, J. Ralston, N. Tanner, N. Wright, J. Smith, R. Price, J. Moor, M. Alexander, A. Lopez, Project THOR: test results for a full-scale, nuclear-compatible ocean world ice penetrator, Eur. Sci. Congr. 2022 (2022), https://doi.org/10.5194/EPSC2022-194.

[14] P. do Vale Pereira, M.J. Durka, B.P. Hogan, K. Richmond, M.W.E. Smith, D. P. Winebrenner, W.T. Elam, B.J. Hockman, A. Lopez, N. Tanner, J. Moor, J. Ralston, M. Alexander, W. Zimmerman, N. Flannery, W. Kuhl, S. Wielgosz, K. L. Cahoy, T.A. Cwik, W.C. Stone, Experimental validation of cryobot thermal models for the exploration of ocean worlds, planet, Sci. J. 4 (2023), https://doi.org/10.3847/PSJ/acc2b7.

[15] N.I. Kömle, P. Tiefenbacher, P. Weiss, A. Bendiukova, Melting probes revisited – ice penetration experiments under Mars surface pressure conditions, Icarus 308 (2018) 117–127, https://doi.org/10.1016/j.icarus.2017.08.006.

[16] N.I. Kömle, P. Tiefenbacher, A. Kahr, Melting probe experiments under Mars surface conditions – the influence of dust layers, CO2-ice and porosity, Icarus 315 (2018), https://doi.org/10.1016/j.icarus.2018.06.012.

[17] M. Treffer, N.I. Kömle, G. Kargl, E. Kaufmann, S. Ulamec, J. Biele, A. Ivanov, O. Funke, Preliminary studies concerning subsurface probes for the exploration of icy planetary bodies, Planet. Space Sci. 54 (2006), https://doi.org/10.1016/j.pss.2006.02.001.

[18] P.G. Talalay, Y. Li, M.A. Sysoev, J. Hong, X. Li, X. Fan, Thermal tips for ice hot-point drilling: experiments and preliminary thermal modeling, Cold Reg. Sci. Technol. 160 (2019) 97–109, https://doi.org/10.1016/j.coldregions.2019.01.015.

[19] E. Kaufmann, G. Kargl, N.I. Kömle, M. Steller, J. Hasiba, F. Tatschl, S. Ulamec, J. Biele, M. Engelhardt, J. Romstedt, Melting and sublimation of planetary ices under low pressure conditions: laboratory experiments with a melting probe prototype, Earth Moon Planets 105 (2009) 11–29, https://doi.org/10.1007/s11038-009-9296-9.

[20] B. Dachwald, J. Mikucki, S. Tulaczyk, I. Digel, C. Espe, M. Feldmann, G. Francke, J. Kowalski, C. Xu, IceMole: a maneuverable probe for clean in situ analysis and sampling of subsurface ice and subglacial aquatic ecosystems, Ann. Glaciol. 55 (2014), https://doi.org/10.3189/2014AoG65A004.

[21] T. Sakurai, H. Chosrowjan, T. Somekawa, M. Fujita, H. Motoyama, O. Watanabe, Y. Izawa, Studies of melting ice using CO2 laser for ice drilling, Cold Reg. Sci. Technol. 121 (2016), https://doi.org/10.1016/j.coldregions.2015.09.014.

[22] M. Mah, A. Kurbatov, S.B. DeFrances, J.A. Randi, J. Talghader, Laser Drilling of Ice, AGUFM, 2018, pp. C41C–1781. https://ui.adsabs.harvard.edu/abs/2018AGUFM.C41C1781M/abstract. (Accessed 25 May 2025).

[23] B. Dachwald, C. Xu, M. Feldmann, E. Plescher, Development of a novel subsurface ice probe and testing of the first prototype on the morteratsch Glacier, Geophys. Res. Abstr. 13 (2011) 4943.

[24] W.C. Stone, B. Hogan, V. Siegel, S. Lelievre, C. Flesher, Progress towards an optically powered cryobot, Ann. Glaciol. 55 (2014), https://doi.org/10.3189/2014AoG65A200.

[25] K. Konstantinidis, C.L.F. Martinez, B. Dachwald, A. Ohndorf, P. Dykta, P. Bowitz, M. Rudolph, I. Digel, J. Kowalski, K. Voigt, R. Förstner, A lander mission to probe subglacial water on Saturn's moon Enceladus for life, Acta Astronaut. 106 (2015), https://doi.org/10.1016/j.actaastro.2014.09.012.

[26] R.D. Lorenz, Thermal drilling in planetary ices: an analytic solution with application to planetary protection problems of radioisotope power sources, Astrobiology 12 (2012), https://doi.org/10.1089/ast.2012.0816.

[27] L. French, F.S. Anderson, F. Carsey, G. French, A.L. Lane, P. Shakkottai, W. Zimmerman, Cryobots: an answer to subsurface mobility in planetary icy environments, in: Proc. ISAIRAS Montr., St-Hubert, 2001.

[28] G.J. Consolmagno, Ice-rich moons and the physical properties of ice, J. Phys. Chem. 87 (1983) 4204–4208, https://doi.org/10.1021/J100244A045/ASSET/J100244A045.FP.PNG_V03.

[29] W.M. Grundy, R.P. Binzel, B.J. Buratti, J.C. Cook, D.P. Cruikshank, C.M. Dalle Ore, A.M. Earle, K. Ennico, C.J.A. Howett, A.W. Lunsford, C.B. Olkin, A.H. Parker, S. Philippe, S. Protopapa, E. Quirico, D.C. Reuter, B. Schmitt, K.N. Singer, A. J. Verbiscer, R.A. Beyer, M.W. Buie, A.F. Cheng, D.E. Jennings, I.R. Linscott, J. W. Parker, P.M. Schenk, J.R. Spencer, J.A. Stansberry, S.A. Stern, H.B. Throop, C.C. C. Tsang, H.A. Weaver, G.E. Weigle, L.A. Young, Surface compositions across Pluto and Charon, Science (2016) 351, https://doi.org/10.1126/SCIENCE.AAD9189/SUPPL_FILE/GRUNDY.SM.PDF.

[30] J.P. Bibring, Y. Langevin, F. Poulet, A. Gendrin, B. Gondet, M. Berthé, A. Soufflot, P. Drossart, M. Combes, G. Bellucci, V. Moroz, N. Mangold, B. Schmitt, S. Erard,

O. Forni, N. Manaud, G. Poulleau, T. Encrenaz, T. Fouchet, R. Melchiorri, F. Altieri, V. Formisano, G. Bonello, S. Fonti, F. Capaccioni, P. Cerroni, A. Coradini, V. Kottsov, N. Ignatiev, D. Titov, L. Zasova, N. Mangold, P. Pinet, B. Schmitt, C. Sotin, E. Hauber, H. Hoffmann, R. Jaumann, U. Keller, R. Arvidson, J. Mustard, T. Duxbury, F. Forget, Perennial water ice identified in the south polar cap of Mars, Nature 428 (2004) 627–630, https://doi.org/10.1038/NATURE02461;KWRD=SCIENCE.

[31] G. Cardell, M.H. Hecht, F.D. Carsey, H. Engelhardt, The subsurface ice probe (SIPR): a low-power thermal probe for the martian polar layered deposits, in: Lunar Planet. Sci. XXXV Mission. InstrumentsHopes Hope Fulfilled, 2004.

[32] S.K. Meerdink, S.J. Hook, D.A. Roberts, E.A. Abbott, The ECOSTRESS spectral library version 1.0, Remote Sens. Environ. 230 (2019), https://doi.org/10.1016/j.rse.2019.05.015.

[33] A.M. Baldridge, S.J. Hook, C.I. Grove, G. Rivera, The ASTER spectral library version 2.0, Remote Sens. Environ. 113 (2009), https://doi.org/10.1016/j.rse.2008.11.007.

[34] S.G. Warren, R.E. Brandt, Optical constants of ice from the ultraviolet to the microwave: a revised compilation, J. Geophys. Res. Atmos. 113 (2008) 1–10, https://doi.org/10.1029/2007JD009744.

[35] F.J. Foss, N.E. Putzig, B.A. Campbell, R.J. Phillips, 3D imaging of Mars' polar ice caps using orbital radar data, Lead. Edge 36 (2017), https://doi.org/10.1190/tle36010043.1.

[36] C.C. Porco, P. Helfenstein, P.C. Thomas, A.P. Ingersoll, J. Wisdom, R. West, G. Neukum, T. Denk, R. Wagner, T. Roatsch, S. Kieffer, E. Turtle, A. McEwen, T. V. Johnson, J. Rathbun, J. Veverka, D. Wilson, J. Perry, J. Spitale, A. Brahic, J. A. Burns, A.D. DelGenio, L. Dones, C.D. Murray, S. Squyres, Cassini observes the active south pole of enceladus, Science 311 (2006) 1393–1401, https://doi.org/10.1126/SCIENCE.1123013/ASSET/B37F54E0-B969-4817-BCC9-96196D1DA226/ASSETS/GRAPHIC/311_1393_F6.JPEG.

[37] X. Jia, M.G. Kivelson, K.K. Khurana, W.S. Kurth, Evidence of a plume on Europa from Galileo magnetic and plasma wave signatures, Nat. Astron. 2 (2018) 459–464, https://doi.org/10.1038/S41550-018-0450-Z.

[38] N. Ligier, C. Paranicas, J. Carter, F. Poulet, W.M. Calvin, T.A. Nordheim, C. Snodgrass, L. Ferellec, Surface composition and properties of Ganymede: updates from ground-based observations with the near-infrared imaging spectrometer SINFONI/VLT/ESO, Icarus 333 (2019) 496–515, https://doi.org/10.1016/J.ICARUS.2019.06.013.

[39] W.M. Calvin, R.N. Clark, Modeling the reflectance spectrum of Callisto 0.25 to 4.1 μm, Icarus 89 (1991) 305–317, https://doi.org/10.1016/0019-1035(91)90180-2.

[40] D.M. Murphy, T. Koop, Review of the vapour pressures of ice and supercooled water for atmospheric applications, Q. J. R. Meteorol. Soc. 131 (2005), https://doi.org/10.1256/qj.04.94.

[41] M.A. McGrath, C.J. Hansen, A. Hendrix, K. Retherford, M.A. McGrath, C.J. Hansen, A. Hendrix, K. Retherford, Observations of Europa's Tenuous Atmosphere, AGUFM, 2007, p. P51E. https://ui.adsabs.harvard.edu/abs/2007AGUFM.P51E..07M/abstract. (Accessed 25 May 2025).

[42] N. Ligier, F. Poulet, J. Carter, R. Brunetto, F. Gourgeot, VLT/SINFONI OBSERVATIONS OF EUROPA: NEW INSIGHTS INTO THE SURFACE COMPOSITION, Astron. J 151 (2016) 163, https://doi.org/10.3847/0004-6256/151/6/163.

[43] R.W. Carlson, A Tenuous Carbon Dioxide Atmosphere on Jupiter's Moon Callisto, (n.d.).

[44] S.W. Squyres, Surface temperatures and retention of H2O frost on Ganymede and Callisto, Icarus 44 (1980) 502–510, https://doi.org/10.1016/0019-1035(80)90040-8.

[45] A.L. Broadfoot, M.J.S. Belton, P.Z. Takacs, B.R. Sandel, D.E. Shemansky, J. B. Holberg, J.M. Ajello, S.K. Atreya, T.M. Donahue, H.W. Moos, J.L. Bertaux, J. E. Blamont, D.F. Strobel, J.C. McConnell, A. Dalgarno, R. Goody, M.B. McElroy, Extreme ultraviolet observations from Voyager 1 encounter with Jupiter, Science 204 (1979) 979–982, https://doi.org/10.1126/SCIENCE.204.4396.979.

[46] R.M. Haberle, Solar system/sun, atmospheres, evolution of atmospheres: planetary atmospheres: mars, in: Encycl. Atmos. Sci, second ed., 2015, https://doi.org/10.1016/B978-0-12-382225-3.00312-1.

[47] A.P. Vidmachenko, A.P. Vidmachenko, Thermal properties of the surface of Mars, Prmw (2023) 243–252. https://ui.adsabs.harvard.edu/abs/2023prmw.conf..243V/abstract. (Accessed 25 May 2025).

[48] A.C. Barr, S.M. Milkovich, Ice grain size and the rheology of the martian polar deposits, Icarus 194 (2008) 513–518, https://doi.org/10.1016/J.ICARUS.2007.11.018.

[49] G.A. Neumann, J.F. Cavanaugh, X. Sun, E.M. Mazarico, D.E. Smith, M.T. Zuber, D. Mao, D.A. Paige, S.C. Solomon, C.M. Ernst, O.S. Barnouin, Bright and dark polar deposits on Mercury: evidence for surface volatiles, Science 339 (2013) 296–300, https://doi.org/10.1126/science.1229764.

[50] D.A. Paige, M.A. Siegler, J.K. Harmon, G.A. Neumann, E.M. Mazarico, D.E. Smith, M.T. Zuber, E. Harju, M.L. Delitsky, S.C. Solomon, Thermal stability of volatiles in the north polar region of mercury, Science 339 (2013) 300–303, https://doi.org/10.1126/science.1231106.

[51] A. Pommerol, B. Jost, O. Poch, Z. Yoldi, Y. Brouet, A. Gracia-Berná, R. Cerubini, A. Galli, P. Wurz, B. Gundlach, J. Blum, N. Carrasco, C. Szopa, N. Thomas, Experimenting with mixtures of water ice and dust as analogues for icy planetary material: recipes from the ice laboratory at the University of Bern, Space Sci. Rev. 215 (2019), https://doi.org/10.1007/s11214-019-0603-0.

[52] J. Klinger, G. Eich, A. Bischoff, F. Joó, H. Kochan, K. Roessler, W. Stichlertt, D. Stöffler, "KOSI" comet simulation experiment at dfvlr: sample preparation and the evolution of the 180/160 and the D/H ratio in the ICY component, Adv. Space Res. 9 (1989) 123–125.

[53] O. Poch, A. Pommerol, B. Jost, N. Carrasco, C. Szopa, N. Thomas, Sublimation of water ice mixed with silicates and tholins: evolution of surface texture and reflectance spectra, with implications for comets, Icarus 267 (2016) 154–173, https://doi.org/10.1016/j.icarus.2015.12.017.

[54] R. Feistel, W. Wagner, Sublimation pressure and sublimation enthalpy of H2O ice Ih between 0 and 273.16 K, Geochem. Cosmochim. Acta 71 (2007), https://doi.org/10.1016/j.gca.2006.08.034.

[55] B. Poch, Olivier; Yoldi, Zuriñe; Jost, Vis-NIR Bidirectional Reflection Spectra of Spherical Water Ice Particles for Different Sizes (2 to 100 Mm), Temperatures (173 and 223 K) and Temporal Evolutions, SSHADE/BYPASS+CSS (OSUG Data Center), 2016, https://doi.org/10.26302/SSHADE/EXPERIMENT_OP_20171130_001.

[56] H.W.C. Aamot, Heat transfer and performance analysis of a thermal probe for glaciers, Cold Reg, Res. Eng. Lab. Tech. Rep. 194 (1967).

[57] M.V. Sykes, Infrared views of the solar system from space, in: Encycl. Sol. Syst., 2007, https://doi.org/10.1016/B978-012088589-3/50041-4.

[58] D. Krankowsky, The composition of comets, Int. Astron. Union Circular 116 (1991), https://doi.org/10.1017/s0252921100012744.

[59] M. Choukroun, K. Altwegg, E. Kührt, N. Biver, D. Bockelée-Morvan, J. Drążkowska, A. Hérique, M. Hilchenbach, R. Marschall, M. Pätzold, M.G.G.T. Taylor, N. Thomas, Dust-to-Gas and refractory-to-ice mass ratios of comet 67P/Churyumov-Gerasimenko from rosetta observations, Space Sci. Rev. 216 (2020), https://doi.org/10.1007/s11214-020-00662-1.

[60] M. Pätzold, T.P. Andert, M. Hahn, J.P. Barriot, S.W. Asmar, B. Häusler, M.K. Bird, S. Tellmann, J. Oschlisniok, K. Peter, The nucleus of comet 67P/Churyumov-Gerasimenko - part I: the global view - nucleus mass, mass-loss, porosity, and implications, Mon. Not. Roy. Astron. Soc. 483 (2019), https://doi.org/10.1093/mnras/sty3171.

[61] K.M. Luchsinger, N.J. Chanover, P.D. Strycker, Water within a permanently shadowed lunar crater: further LCROSS modeling and analysis, Icarus 354 (2021), https://doi.org/10.1016/j.icarus.2020.114089.

[62] S. Li, P.G. Lucey, R.E. Milliken, P.O. Hayne, E. Fisher, J.P. Williams, D.M. Hurley, R.C. Elphic, Direct evidence of surface exposed water ice in the lunar polar regions, Proc. Natl. Acad. Sci. USA. 115 (2018), https://doi.org/10.1073/pnas.1802345115.

[63] J. Audouard, F. Poulet, M. Vincendon, R.E. Milliken, D. Jouglet, J.P. Bibring, B. Gondet, Y. Langevin, Water in the Martian regolith from OMEGA/Mars Express, J. Geophys. Res. Planets 119 (2014), https://doi.org/10.1002/2014JE004649.

[64] S. Cull, R.E. Arvidson, M.T. Mellon, P. Skemer, A. Shaw, R.V. Morris, Compositions of subsurface ices at the mars phoenix landing site, Geophys. Res. Lett. 37 (2010), https://doi.org/10.1029/2010GL045372.

[65] J. Zhang, J. Guo, M.I. Dobynde, Y. Wang, R.F. Wimmer-Schweingruber, From the top of Martian olympus to deep craters and beneath: mars radiation environment under different atmospheric and Regolith depths, J. Geophys. Res. Planets 127 (2022), https://doi.org/10.1029/2021JE007157.

[66] G.F. Lindal, G.E. Wood, H.B. Hotz, D.N. Sweetnam, V.R. Eshleman, G.L. Tyler, The atmosphere of Titan: an analysis of the Voyager 1 radio occultation measurements, Icarus 53 (1983), https://doi.org/10.1016/0019-1035(83)90155-0.

[67] P. Talalay, C. Yang, P. Cao, R. Wang, N. Zhang, X. Fan, Y. Yang, Y. Sun, Ice-core drilling problems and solutions, Cold Reg. Sci. Technol. 120 (2015) 1–20, https://doi.org/10.1016/J.COLDREGIONS.2015.08.014.

[68] S. Ulamec, J. Biele, O. Funke, M. Engelhardt, Access to glacial and subglacial environments in the solar system by melting probe technology, life extrem, Environ. Times (2006) 9781402062858, https://doi.org/10.1007/978-1-4020-6285-8_1.

[69] K. Schüller, J. Kowalski, How to Design Efficient Thermal Melting Probes for Subsurface Ice Exploration, AGUFM, 2016, pp. C53B–709. https://ui.adsabs.harvard.edu/abs/2016AGUFM.C53B0709K/abstract. (Accessed 25 May 2025).

[70] I.P. Wright, S.J. Barber, G.H. Morgan, A.D. Morse, S. Sheridan, D.J. Andrews, J. Maynard, D. Yau, S.T. Evans, M.R. Leese, J.C. Zarnecki, B.J. Kent, N.R. Waltham, M.S. Whalley, S. Heys, D.L. Drummond, R.L. Edeson, E.C. Sawyer, R.F. Turner, C. T. Pillinger, Ptolemy - an instrument to measure stable isotopic ratios of key volatiles on a cometary nucleus, Space Sci. Rev. 128 (2007) 363–381, https://doi.org/10.1007/S11214-006-9001-5/METRICS.

[71] M. "Dutch" von Ehrenfried, Perseverance's Design, Perseverance Mars 2020 Mission (2022) 27–74, https://doi.org/10.1007/978-3-030-92118-7_3.